

# **$a_0(980)$ photoproduction at the BGOOD experiment**

Adrian Sonnenschein

Masterarbeit in Physik  
angefertigt im Physikalischen Institut

vorgelegt der  
Mathematisch-Naturwissenschaftlichen Fakultät  
der  
Rheinischen Friedrich-Wilhelms-Universität  
Bonn

Septemeber 2021

I hereby declare that this thesis was formulated by myself and that no sources or tools other than those cited were used.

Bonn, .....  
Date

.....  
Signature

1. Gutachter: Prof. Dr. Hartmut Schmieden
2. Gutachter: Prof. Dr. Ian C. Brock

# Acknowledgements

---

I would like to thank Prof. Dr. Hartmut Schmieden and the working group for making this thesis possible and always keeping a supportive and friendly atmosphere. Furthermore, I have to thank Dr. Thomas Jude, the supervisor of this thesis, who helped a lot with his ideas and knowledge and Dr. Georg Scheluchin for solving a couple of technical problems.



# Contents

---

|          |  |           |
|----------|--|-----------|
| <b>1</b> | <b>Introduction</b>  | <b>1</b>  |
| <b>2</b> | <b>Theoretical Background</b>  | <b>5</b>  |
| 2.1      | Quark model . . . . .  | 5         |
| 2.1.1    | Baryons . . . . .  | 8         |
| 2.1.2    | Mesons . . . . .   | 9         |
| 2.2      | Tetraquarks . . . . .  | 10        |
| 2.2.1    | The scalar nonet . . . . .   | 10        |
| 2.2.2    | Diquark model and molecular model . . . . .  | 12        |
| 2.2.3    | Decay mechanism . . . . .  | 12        |
| 2.3      | The $a_0(980)$ and $a_2(1320)$ . . . . .   | 13        |
| <b>3</b> | <b>The BGOOD Experiment</b>  | <b>15</b> |
| 3.1      | ELSA . . . . .   | 15        |
| 3.1.1    | LINACs . . . . .   | 15        |
| 3.1.2    | Booster Synchrotron . . . . .  | 16        |
| 3.1.3    | Stretcher Ring . . . . .   | 16        |
| 3.2      | BGOOD . . . . .  | 17        |
| 3.2.1    | Tagger-System . . . . .  | 17        |
| 3.2.2    | Central detector . . . . .   | 20        |
| 3.2.3    | Intermediate detector . . . . .  | 23        |
| 3.2.4    | Forward detector . . . . .   | 23        |
| <b>4</b> | <b>Basic methods of particle identification</b>  | <b>27</b> |
| 4.1      | The EXPLORA framework . . . . .  | 27        |
| 4.2      | Track building at BGOOD . . . . .  | 28        |
| <b>5</b> | <b>Event selection for the <math>\gamma p \rightarrow \pi^0 \eta p</math> reaction</b>               | <b>33</b> |
| 5.1      | Identification of the Proton . . . . .   | 33        |
| 5.2      | Identification of the $\pi^0$ and $\eta$ meson . . . . .   | 33        |
| 5.3      | Combined Selection . . . . .   | 37        |
| <b>6</b> | <b>Data analysis</b>   | <b>41</b> |
| 6.1      | Background Separation . . . . .  | 41        |
| 6.2      | Determination of the differential cross section . . . . .  | 42        |
| 6.2.1    | Systematic uncertainties . . . . .   | 45        |
| 6.2.2    | Differential cross section of the uncorrelated $\gamma p \rightarrow \pi^0 \eta p$ channel . . . . . | 46        |

|          |   |           |
|----------|---|-----------|
| 6.2.3    | Differential cross section of the $\gamma p \rightarrow a_0(980)p \rightarrow \pi^0 \eta p$ channel . . . . . | 46        |
| <b>7</b> | <b>Summary and outlook</b>  | <b>49</b> |
|          | <b>Bibliography</b>   | <b>51</b> |

## Introduction

---

The main goal of physics is to capture and describe the behaviour of our universe with mathematical formulas and models. Since the beginning up until today one of the most important areas of interest is the structure and interaction of matter. The first consideration of matter as tiny, unbreakable particles dates way back to the ancient Greeks shaping the term *átomos*, the consolidation of the theory by fundamental experiments started at the end of the 18th century. In trailblazing studies in the early 20th century Rutherford, Bohr and other prestigious physicists were able to verify the proton as heavy, positively charged center of the atom surrounded by small, negatively charged electrons assigned to fixed orbits. Years later, as physics progresses, the neutron was experimentally discovered as nearly equal heavy, uncharged partner of the proton in the atomic core. Advanced technology in the sector of particle acceleration allowed to set a new milestone in the mid/late 60s. In deep inelastic electron-nucleon scattering experiments it turns out the nucleons consist of even smaller particles. The substructure was previously described by Murray Gell-Man and George Zweig in the quark model, bringing order to the so called 'particle zoo'. All of these results and many more can be summed up in today's standard model of particle physics (figure 1.1), consisting of six types of quarks (up, down, strange, charm, top, bottom), six leptons (electron, myon, tauon and their corresponding neutrinos), twelve exchange particles of the strong-, weak- and electromagnetic interaction (eight gluons,  $W^\pm$ - and Z-bosons and the photon) and last but not least the Higgs boson, whose existence was experimentally proven in 2012 at the LHC<sup>1</sup>.

But research has not come to an end yet. The standard model, as good as it is, yet excludes essential areas like the gravitational force, as well as dark matter and dark energy physics. Furthermore it does not always match with reality, exemplary in the case of the matter antimatter asymmetry and its pending predictions has to be investigated.

The above mentioned constituent quark model, included in the framework of the standard model, defines hadrons as colour neutral, bound states composed of either a quark-antiquark-pair (*meson*) or three quarks (*baryon*) constrained by the confinement of the strong force at low energies. Particles arising from this concept have been studied in-depth and are successfully classified in SU(N) flavour multiplets, however the observed spectra can not be considered understood completely. In baryon spectroscopy less resonances than expected have been found, also referred to as *missing resonances*

---

<sup>1</sup> Large Hadron Collider

*problem*, whereas in meson spectroscopy additional states have been measured. A solution to the proliferation of states is provided by QCD, allowing for more complex, so called *exotic* states beyond the constituent quark model. Apparent are multi-quark combinations like tetraquarks ( $qq\bar{q}\bar{q}$ ), pentaquarks ( $qqqq\bar{q}$ ) and hexaquarks ( $qqq\bar{q}\bar{q}\bar{q}$ ), as well as glueballs ( $gg$ ), enabled by the self interaction of gluons and last but not least hybrid states ( $q\bar{q}g$ ).

Considering the approach from a conservative perspective, these states have to be experimentally proven. In recent years hadron spectroscopy experienced a renaissance by accomplishing that and discovering tetra- and pentaquark systems including c and b quarks, the most prominent probably being the  $\chi_{c1}(3872)$  in the charm sector, first observed in 2003 at BELLE[1]. Similar structures are expected in the sector of light u,d,s quarks. The BGOOD<sup>2</sup> experiment at the ELSA<sup>3</sup> facility of the Rheinische Friedrich-Wilhelms-Universität Bonn is excellently suited for the investigation in the latter regime, operating at beam energies up to 3.2 GeV, which allow for photoproduction of light mesons close to production threshold and beyond. It comprises a high resolution, large acceptance EMC in the central part of the detector system, optimized to measure neutral meson decays, as well as a forward spectrometer well designed to detect the charged particles. In this context the thesis analyses data from the 2017 beam time of the BGOOD experiment, searching for two promising, long predicted tetraquark candidates, the isovector resonances  $a_0(980)$ , located slightly below the production threshold of  $K\bar{K}$  as well as the  $a_2(1320)$ . Photoproduction of a  $\pi^0\eta$  pair off a proton ( $\gamma p \rightarrow \pi^0\eta p$ ) is a favourable reaction channel for observation, since both candidates have a dominant neutral decay mode that should contribute to the  $\pi^0\eta$  invariant mass spectrum at a certain energy range. Important goals are to study their reaction mechanisms in photoproduction, determine their cross sections and disentangle them from other broad and overlapping resonances in the light quark sector.

It should be noted that several major experimental setups like GrAAL<sup>4</sup>, A2, CB-ELSA<sup>5</sup>/TAPS and CLAS<sup>6</sup> managed to take high-quality data of the photoproduction of  $\pi^0$  and  $\eta$ . However, recent publications of the first three mainly focus on the sequential decay of heavier baryon resonance where the intermediate states  $\Delta^+(1232)\eta$ ,  $N^+(1535)\pi^0$  and  $p a_0(980)$  contributing to the reaction channel[2][3][4], while CLAS is more pinpointed to the  $a_2(1320)$  photoproduction due to their high beam energies[5]. Moreover, a theoretical approach (detailed in section 2.2) interpret states like the  $a_0(980)$  and  $a_2(1320)$  as a molecular like system of two conventional mesons where the constituents are only lightly bound among themselves. In this case in photoproduction a small momentum transfer from the initial photon to the tetraquark system should be helpful. The proton then must receive the main portion of the momentum, resulting in very forward directions, whereas the residual hadronic tetraquark system is kept intact and decays nearly at rest. The BGOOD experiment promotes this special kinematic by its ability to measure the proton at more forward angles and is consequently complementary in coverage to the other experiments mentioned above[6].

---

<sup>2</sup> Bismuth Germanate Oxide - Open Dipole

<sup>3</sup> Electron Stretcher Accelerator

<sup>4</sup> Grenoble Anneau Accélérateur Laser

<sup>5</sup> Crystal Barrel at ELSA

<sup>6</sup> CEBAF Large Acceptance Spectrometer in Hall B at Jefferson Laboratory



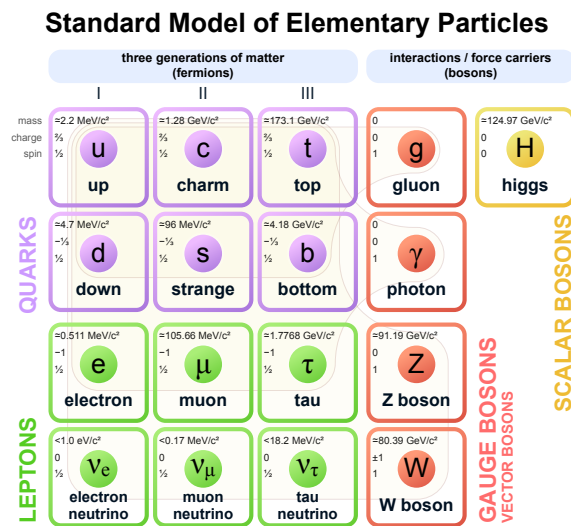


Figure 1.1: Standard model of particle physics[7].



## Theoretical Background

### 2.1 Quark model

As mentioned in the introduction the quark model was invented, enhanced by the discovery of the substructure of both nucleons, to systematically organize the variety of strongly interacting particles, the hadrons, based on the properties (charge, mass, magnetic moment, isospin, ...) of their constituents. The quark model representation of hadrons is implemented in QCD, the theory of strong interactions. QCD serves basis for the model, describing hadrons as bound states of quarks and gluon fields. The quarks can be assigned to the *fermions* (particles with half odd integer spin), whereas the gluons are gauge *bosons* (particles with integer spin). As the gluons carry no intrinsic quantum numbers beyond colour charge, that is believed to be permanently confined, constituent quarks and antiquarks are responsible for the quantum numbers of hadrons, which strongly emphasizes the role of the minimum-quark-content part of its wave function.

**Quarks** The quarks, initially named partons, are classified into six different types of flavour, u (*up*), d (*down*), s (*strange*), c (*charm*), t (*top*) and b (*bottom*). Further the categorisation into three doublets, also called generations, based on their mass is possible, increasing from left to right:

$$\begin{pmatrix} u \\ d \end{pmatrix} \quad \begin{pmatrix} c \\ s \end{pmatrix} \quad \begin{pmatrix} t \\ b \end{pmatrix}.$$

It should be noted, that the more heavy quarks were discovered later than the light ones, the top quark only in 1995, enabled by accelerators with higher center of mass energies. Also the fractional charge of the quarks (upper row +2/3, lower row -1/3) was not determined right away by investigating nucleons, but results from other indications, like the existence of hadrons with double positive charge, yet not with double negative. The charge is correctly calculated by the generalized Gell-Mann-Nishijima formula

$$Q = I_z + \frac{Y}{2} \quad \text{with: } Y = \mathcal{B} + S + C + B + T \quad (2.1)$$

where  $\mathcal{B}$  is the baryonnumber,  $S$  the strangeness,  $C$  the charm,  $B$  the bottomness and  $T$  the topness. The individual quantum numbers are listed in table 2.1 along with the isospin quantum numbers of the quarks. Beside the fundamental quantities energy  $E$ , momentum  $p$ , angular momentum  $L$ , charge  $Q$ , baryon number  $\mathcal{B}$  and lepton number  $l$  the strong interaction further conserves the  $CP$ -symmetry,

|     | Q    | I   | $I_z$ | S | C | B | T | $\mathcal{B}$ | Spin | Colour | Mass                       |
|-----|------|-----|-------|---|---|---|---|---------------|------|--------|----------------------------|
| $d$ | -1/3 | 1/2 | -1/2  | 0 | 0 | 0 | 0 | 1/3           | 1/2  | r,g,b  | $4.67^{+0.48}_{-0.17}$ MeV |
| $u$ | 2/3  | 1/2 | 1/2   | 0 | 0 | 0 | 0 | 1/3           | 1/2  | r,g,b  | $2.16^{+0.49}_{-0.26}$ MeV |
| $s$ | -1/3 | 0   | 0     | 1 | 0 | 0 | 0 | 1/3           | 1/2  | r,g,b  | $93^{+11}_{-5}$ MeV        |
| $c$ | 2/3  | 0   | 0     | 0 | 1 | 0 | 0 | 1/3           | 1/2  | r,g,b  | $1.27 \pm 0.02$ GeV        |
| $b$ | -1/3 | 0   | 0     | 0 | 0 | 1 | 0 | 1/3           | 1/2  | r,g,b  | $4.18^{+0.03}_{-0.02}$ GeV |
| $t$ | 2/3  | 0   | 0     | 0 | 0 | 0 | 1 | 1/3           | 1/2  | r,g,b  | $172.76 \pm 0.30$ GeV      |

Table 2.1: Properties of the quarks[8]

colour, flavour and the absolute value of the isospin. The isospin  $I$  represents the inner symmetry under the strong interaction. Initially introduced to distinguish proton and neutron as differently charged states of the nucleon  $I$  is formally treated like a quantum mechanical angular momentum, where the  $I_z$ -component represents the eigenvalue. The formalism can be applied to all strong interacting particles. Aside from opposite charge, flavour and baryon quantum number the  $I_z$  is reversed as well for antiquarks. Mass  $m$  and spin  $S$  are maintained.

**Gluons** Our idea of a fundamental interaction is always associated with an exchange of particles, in case of the strong interaction these particles are the gluons. Similar to the photon in QED, coupling to the electric charge, the gluon is a  $J^P = 1^-$  vector boson that couples to the *colour* charge. Colour comes in three types,  $r$  (red),  $b$  (blue) and  $g$  (green), originated from theoretical considerations to save the Pauli exclusion principle for baryons. Pauli principle states that two or more identical fermions can not occupy the same quantum state within a quantum system simultaneously, the wave function (for baryons shown in eqn. 2.5) has to be antisymmetric concerning interchange. For instance this would not be the case for the  $\Delta^{++}$ , consisting of three up-quarks with parallel spin and  $l = 0$ , without colour charge. The hypothesis of colour factor being three can be experimentally confirmed by determining the ratio of cross section for pair production of quarks compared to muons.

While every quark possesses a colour (and every antiquark an anticolour) gluons themselves carry both colour and anticolour at the same time, allowing for selfinteraction, contrary to photons not carrying electric charge. According to the rules of group theory, the  $3 \otimes 3$  colour combinations form a completely symmetric singlet and an antisymmetric octet. From the octet every colour state can be build up, how it is composed is a matter of convention. One possible choice is:

$$r\bar{b}, \quad r\bar{g}, \quad b\bar{r}, \quad b\bar{g}, \quad g\bar{r}, \quad g\bar{b}, \quad \sqrt{1/2}(r\bar{r} - g\bar{g}), \quad \sqrt{1/6}(r\bar{r} + g\bar{g} - 2b\bar{b}) \quad (2.2)$$

The singlet on the other hand is invariant under rotation in colour space:

$$\sqrt{1/3}(r\bar{r} + g\bar{g} + b\bar{b}) \quad (2.3)$$

It has no effective netto colour charge and therefore would not be exchanged between coloured particles. The regulation of confinement, explained in the following section, could not be applied

either, so the interaction range would be infinite. For these reasons it does not occur in nature.

**Strong coupling constant  $\alpha_s$**  The strength of an interaction can be defined by the coupling strength of the associated exchange particles, characterized by a coupling constant. For the strong interaction this constant changes dynamical, heavily depended on the squared momentum transfer  $Q^2$ . While propagating in space gluons perform field fluctuations, similar to photons in QED. These pair production and pair annihilation of quarks screen from the charges of the extra virtual particles, or interactions between these virtual particles. However, due to the selfinteraction of the gluons, they can produce additional gluons, resulting in a sort of anti-screening. In first order of perturbation theory this effect leads to a coupling constant of:

$$\alpha_s(Q^2) = \frac{12\pi}{(33 - 2n_q) \cdot \ln(Q^2/\Lambda^2)} \quad (2.4)$$

Here  $n_q$  is the number of participating quark flavour types. It varies depending on  $Q^2$ , due to virtual quark-antiquark-pairs from the three heavier quarks only contribute at small distances because of their short lifetime. The parameter  $\Lambda$  works as a measuring scale, within QCD can be dealt with by perturbation theory. It can be shifted and is estimated in the range about  $\Lambda \approx 250 \text{ MeV}/c$  by renormalisation scheme and experimental results. As shown in figure 2.1 at close distances, corresponding to a large  $Q^2$ , strong interacting particles perceive little charge and the coupling constant decreases asymptotically, while at large distances the behaviour is contrary. Therefore, quarks exclusively occur in bound systems, mesons and baryons, from which they can not be removed from (*confinement*). In case of separation the energy of the field tube of the strong interaction growth up to a point where its favourable to break the QCD strings and a light quark-antiquark pair is created. At short distances quarks can be considered as free (*asymptotic freedom*).

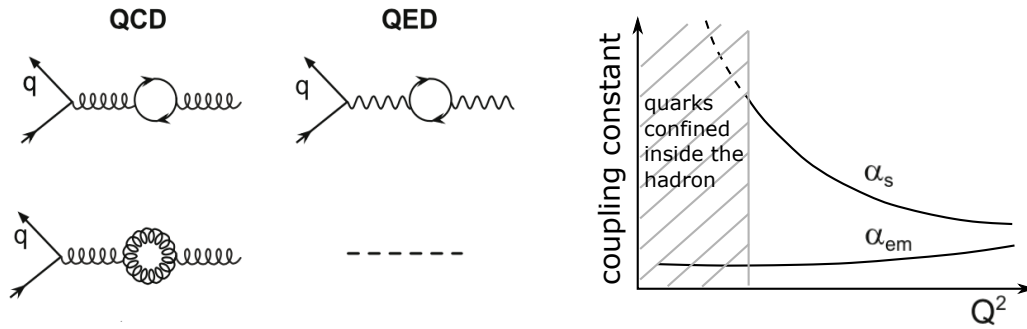


Figure 2.1: On the left side Feynman diagrams of quantum fluctuation of gluon and photon. On the right side the qualitative  $Q^2$  dependence of the strong and electromagnetic coupling constant. The change of the constant, also called *running*, is very weak for  $\alpha_{em}$ , increasing only slightly from 1/137 (fine-structure constant) at low energies.[9]

**Hadrons as colour neutral objects** Colour offers a new degree of freedom, so it could be expected to witness hadrons in all sorts of colour configurations based on the quarks they are constituted of, but there is only one kind of each hadron observed. This leads to the conclusion that free, isolated particles have to be colour neutral, coinciding with the fact that free quarks do not exist. Considering the composition of hadrons a colour neutral or white state is formed by either a combination of colour and anticolour or a mix of all three colours. Consequently a gluon coupling between two quarks has to transfer its colour and anticolour in a way that the colour neutral of the hadron state is maintained.

### 2.1.1 Baryons

Baryons are composed of three valence quarks, exclusively responsible for the quantum numbers, as well as additional gluons and quark-antiquark-pairs emerging and annihilating in the presence of the strong field, that carry part of the momentum and mass. The baryon numbers of the three valence quarks adding up to  $\mathcal{B} = 1$  (respectively  $\mathcal{B} = -1$  for antibaryons). All other particles have a baryon number of  $\mathcal{B} = 0$ . Because of the quarks possessing a spin of  $1/2$ , the baryons must be fermions as well with either a half integer spin of  $1/2$  or  $3/2$  depending on the spin configuration of the quarks. For baryon ground states with no orbital angular momentum ( $L = 0$ ) this corresponds to the total angular momentum  $J$  of the baryon. The parity is directly related to the angular momentum by  $P = (-1)^L$ , due to the baryon only carrying quarks, which have a positive parity by convention, no antiquarks with negative parity. The wave function must be antisymmetric under interchange of any two equal-mass quarks. This is accomplished by the colour part, a completely antisymmetric SU(3) singlet of the three colours:

$$|qqq\rangle_A = |\text{color}\rangle_A \times |\text{space, spin, flavor}\rangle_S \quad (2.5)$$

There are many possible combinations for the diverse quark flavour types to form a baryon, accordingly there are many different baryons. An ordering scheme can be made up by group theory. Taking the three lightest quarks  $u$ ,  $d$  and  $s$  into account a flavour symmetry group SU(3) arises, forming the following multiplets:

$$\mathbf{3} \otimes \mathbf{3} \otimes \mathbf{3} = \mathbf{10}_S \oplus \mathbf{8}_M \oplus \mathbf{8}_M \oplus \mathbf{1}_A \quad (2.6)$$

The subscripts indicate symmetric, mixed-symmetry, or antisymmetric states. With respect to the spin the model can be extended to an approximate flavor-spin SU(6), by assigning an up- or down spin to each quark:

$$\mathbf{6} \otimes \mathbf{6} \otimes \mathbf{6} = \mathbf{56}_S \oplus \mathbf{70}_M \oplus \mathbf{70}_M \oplus \mathbf{20}_A \quad \text{with: } \mathbf{56}_S = \mathbf{10}^4 \oplus \mathbf{8}^2 \quad (2.7)$$

Here the index  $(2S + 1)$  of the  $\mathbf{56}_S$  gives the net spin  $S$  of the quarks for each particle in the SU(3) multiplet. The decuplet with quantum numbers  $J^P = 3/2^+$  represents the ten possible states with a completely symmetric single spin- and flavour wave function. The spins have to be aligned parallel, for the flavour wave function of states without purely identical flavour content multiple terms necessarily have to be symmetric. The octet with quantum numbers  $J^P = 1/2^+$  covers the states with mixed-symmetric single spin- and flavour wave functions complementing each other for a completely symmetric spin-flavour wave function. The  $\mathbf{70}_M$  and  $\mathbf{20}_A$  require some excitation of the spatial part of the wave function to satisfy the requirement of an overall antisymmetric wave function and are not covered here.

Further extension of the flavour symmetry to SU(4) or even SU(5) can be done by adding the charm-

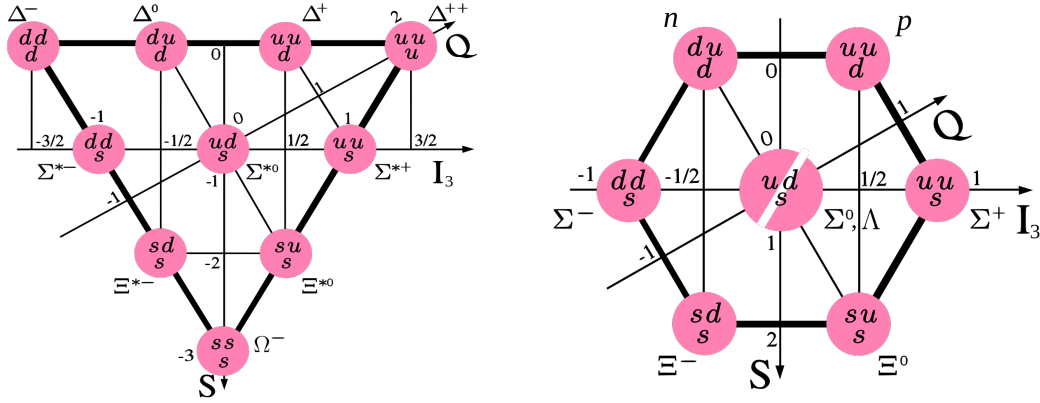


Figure 2.2: Baryons of the  $J^P = 3/2^+$  decuplet (left) and the  $J^P = 1/2^+$  octet (right) ordered by the third component of isospin  $I_3$  and strangeness  $S$ . Antibaryons form equivalent multiplets but with antiquarks content[10].

and/or the bottom-quark, resulting in larger multiplets. However, due to the large mass difference compared to the light quarks this symmetry is even more strongly broken than the  $SU(3)$ . The top quark can be excluded for the present, as baryon states with a top quark are unlikely considering their short lifetime.[8]

### 2.1.2 Mesons

Mesons are composed of a quark-antiquark-combination, leading to possible spin configurations of 0 (antiparallel spins) and 1 (parallel spins). The total angular momentum value  $J$  is then located in the range  $|L - S| \leq J \leq |L + S|$  limited by the contribution of the orbital angular momentum  $L$ . Unlike the baryon parity the meson parity is defined by  $L$  by  $P = (-1)^{L+1}$  due to the antiquarks negative intrinsic parity. Mesons with quark-antiquark content of the same flavour, thus being their own antiparticle, are further characterized by the charge parity quantum number  $C = (-1)^{L+S}$ , defining their behaviour under the symmetry operation of charge conjugation. The charge conjugation operator changes the sign of all quantum charges, therefore, transforms a particle into its antiparticle. The double application reconstitutes the original state. A generalization to the G-parity  $G = (-1)^{I+L+S}$  can be made by taking the charged  $u\bar{d}$  and  $d\bar{u}$  states into account.

Because of the quantum numbers being regulated by the rules above, there are only certain combinations of natural spin-parity and C-parity possible inside the  $q\bar{q}$ -model. Allowed are states with  $J^{PC}$  quantum numbers  $0^{-+}, 0^{++}, 1^{--}, 1^{+-}, 1^{++}, 2^{++}, \dots$ , and so on. A summary with the individual configuration is given in table 2.3. Mesons with quantum states differing from the scheme, in particular  $0^{-+}, 0^{+-}, 1^{-+}, 2^{+-}, 3^{-+}, \dots$ , also called *exotic* mesons, lie outside of the model and must be composed differently (e.g. tetraquarks in the section below).

Similar to the baryons mesons are classified in multiplets as well. With respect to the quark flavour of the three light quarks and antiquarks the group theory of  $SU(3)$  symmetry, as we already known from the gluons, forms nine states within an octet and a singlet. These are shown in figure 2.3 for the pseudoscalar mesons. It should be mentioned, that the eigenstates of isoscalar mesons with the

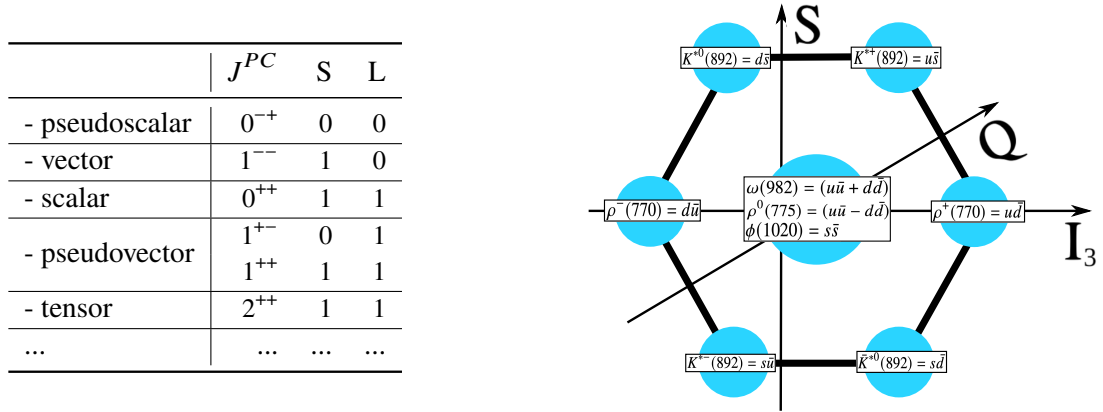


Figure 2.3: Possible combinations of  $J^{PC}$  quantum numbers for mesons within the  $q\bar{q}$ -model (left) and the lightest meson nonet (right), formed by the vector mesons and sorted by the third component of isospin  $I_3$  and strangeness  $S$  [11].

same  $J^{PC}$  mix, due to the electroweak interaction transforming quark flavours. As one of these are respectively part of the octet and the other one of the singlet, they can be expressed by a linear combination of the wave function, exemplary for the pseudoscalar nonet with  $\eta$  and  $\eta'$ . This looks like:

$$\begin{pmatrix} \cos \theta_p & -\sin \theta_p \\ \sin \theta_p & \cos \theta_p \end{pmatrix} \begin{pmatrix} \eta_8 \\ \eta_1 \end{pmatrix} = \begin{pmatrix} \eta \\ \eta' \end{pmatrix} \quad \text{with:} \quad \begin{aligned} \eta_8 &= (u\bar{u} + d\bar{d} - 2c\bar{c})/\sqrt{6} \\ \eta_1 &= (u\bar{u} + d\bar{d} + c\bar{c})/\sqrt{3} \end{aligned} \quad (2.8)$$

with  $\theta_p$  as mixing angle. For the  $\eta$  and  $\eta'$  this angle is fairly small, therefore they are approximately pure octet  $\eta_8$  and singlet  $\eta_1$  states. However, for the higher, more excited nonets the mixing gets stronger (e.g the vector meson mixing angle  $\theta_v$  is close to ideal, resulting in the  $\phi$  to be nearly pure  $s\bar{s}$ ). Extension of the flavour symmetry analogously to the baryon sector unlocks isoscalar charmonium and bottomonium states like  $\eta_c$  and  $\eta_b$  in the pseudoscalar case, nevertheless the mixing with the light quark states is negligible here, due to the huge mass difference [8].

## 2.2 Tetraquarks

### 2.2.1 The scalar nonet

The previous chapter explains the formation of the baryon and meson and their classification in multiplets, based on the constituent quark model. This works successfully regarding the spatial ground states of the flavour SU(3) symmetry of the light quarks, however, slowly starts to fall apart for spatially excited states. Regarding even the first excitation in orbital angular momentum, there exist many mesons below 2 GeV, which can not be accommodated in the conventional  $q\bar{q}$ -nonets.

The deviation from the model can be easily verified by looking at the scalar nonet ( $0^{++}$ ), which should include the lightest scalar mesons  $f_0(500)$ ,  $\kappa(800)$ ,  $a_0(980)$  and  $f_0(980)$ . Assuming the flavour content in the ideal mixing limit could be written identical to the vector mesons (shown in fig. 2.4(a)) these are predicted to be located in a mass region above 1.2 GeV, due to carrying one unit of orbital angular momentum. This would be consequently heavier than the vector mesons nonet, whose



lightest member weighs even more than the  $f_0(500)$ . Nevertheless the properties and behaviour of

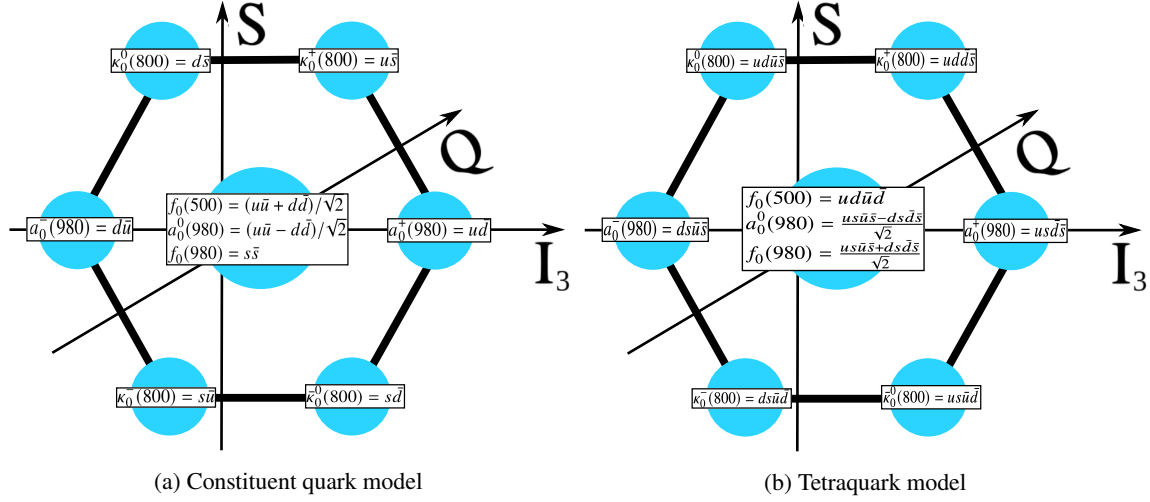


Figure 2.4: Configurations of the scalar nonet in ideal mixing limit (based on[12]).

these particles indicate a flavour composition apart from this one. Despite possessing strange flavour content the mass of the isoscalar  $a_0(980)$  is degenerated with the heavier isovector  $f_0(980)$  instead of being close to mass range of the lighter isovector  $f_0(500)$ , like the corresponding  $\rho$ - and  $\omega$ -meson in the comparable vector nonet. A third evidence that advocates against the classic model are the decay modes and of the  $f_0(980)$  and  $a_0(980)$ . Considering the  $f_0(980)$  as a  $s\bar{s}$ -state, the strong decay  $f_0(980) \rightarrow \pi\pi$  is possible but heavily suppressed by the OZI<sup>1</sup>-rules, which by its mechanism inhibits a decay only enabled by the entire annihilation and creation of quark lines. Yet it is experimentally determined to be the dominant decay channel. Likewise, the decay channel  $\phi \rightarrow f_0(980)\gamma$  should be preferred over the OZI and isospin violating  $\phi \rightarrow a_0(980)\gamma$ , however the branching fraction of the second channel does not vanish and is not as separated as expected from the first one[8][12].

A solution to the problems can be made up by the picture of tetraquark, initially suggested by Robert L. Jaffe in 1977 based on a semi-classical approximation to the MIT quark-bag model[13]. He suggests these states to be a strongly bound scalar diquarks and antidiquarks in relative S-wave. Other physicists like J. D. Weinstein and N. Isgur[14], G. Janssen[15] and J. A. Oller, E. Oset and A. Ramos[16] later interpret them as dynamically generated states from meson-meson interactions with a molecular like bonding, the strengths and weaknesses of the different models are discussed in the next subsection.

In the ideal mixing limit the states can be written as shown in fig. 2.4(b). Jaffe describes this tetraquark multiplet as the  $0^+$  cryptoexotic nonet where the light mass of the particles is originated from attractive gluon-magnetic interactions like for the pseudoscalar mesons, while the phenomenology of mixing induced by the quarks kinetic-energy operator is quite different in the tetraquark sector compared to the classic quark-antiquark mesons. According to this interpretation the isosinglet  $f_0(980)$  is degenerated with the isotriplet  $a_0(980)$  and the light  $f_0(500)$ , analogue of the  $\phi$ , contains no strange quarks. Now the inverted mass spectrum as well as the branching fractions can be understood. Moreover, this

<sup>1</sup> Okubo-Zweig-Iizuka

makes room for a conventional quark-antiquark-nonet, whose mesons  $f_0(1370)$ ,  $a_0(1450)$ ,  $K_0^*(1430)$  and  $f_0(1500)$  are then located in the expected mass region.

### 2.2.2 Diquark model and molecular model

When experimental investigation of exotic multi-quark states progressed and the first candidates were discovered, two different interpretations about the correct picture of matter arose. The first one, favoured by Jaffe, wanted to describe them as a completely new stand-alone particle type using a model of two tightly bound colour-charged diquarks overlapping in the same small volume of space. As both diquark pairs have net colour they have to fuse as a compact, colour-neutral particle for an instant before switching partners and dissociating. The other model chooses a more conservative approach, defining the states to be short-term resonances of two colour-neutral mesons with a molecular like bonding. The models are graphically displayed in figure 2.5.

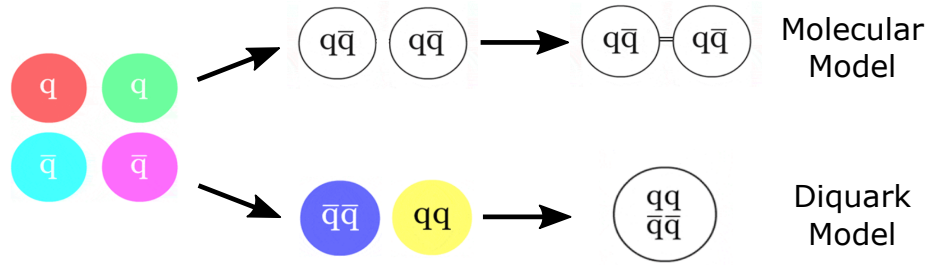


Figure 2.5: Graphical representation of the molecular model and of the diquark model (based on[17]).

The main argument against the meson molecule theory is their appearance in high-energy collision experiments, despite QCD considering the mesons to bound loosely. Critics like Antonio Polosa, theorist at Sapienza University of Rome, compare this to a "crystal glass" inside a "nuclear explosion"[17]. On the other hand wave functions of many candidates appear to consist, at least in part, of pairs of  $q\bar{q}$ -mesons. Resonances with their mass almost exactly at the production threshold of two conventional  $q\bar{q}$ -mesons therefore strongly support the meson molecule theory[18]. In case of the  $a_0$  this would be the  $K\bar{K}$  threshold. An other example is the  $\chi_{c1}(3872)$ , mentioned in the introduction, which is close to the  $D^0\bar{D}^{0*}$  threshold. The model was subsequently favoured until the discovery of the  $Z_c(4430)$  in 2007 by the Belle collaboration and confirmation in 2014 at LHCb<sup>2</sup>, whose characteristics like mass and spin-parity do not match up with any two conventional mesons. The discovery pushes physicists to extend their simple picture of quark interactions, an explanation integrating both phenomena is not found yet.

### 2.2.3 Decay mechanism

Beside his concept about the construction of tetraquarks Robert L. Jaffe takes a closer look at their decay mechanism. He states that if not prohibited by the mass, a S-wave tetraquark state will be unstable against a decay into two conventional color-singlet S-wave mesons in relative S-waves. Considering the Feynman diagrams in figure 2.6, such a decay would be not only be OZI-allowed,

<sup>2</sup> Large Hadron Collider beauty

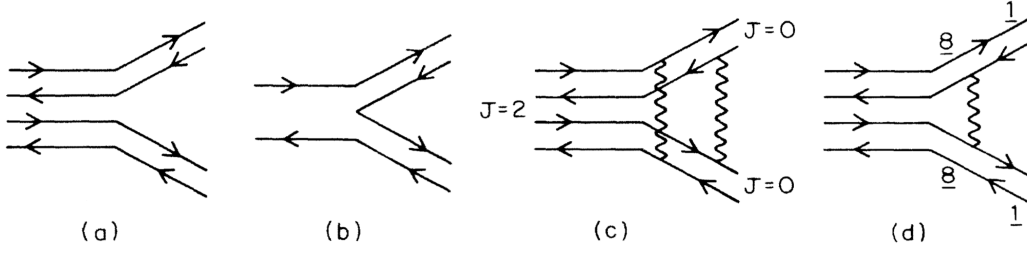


Figure 2.6: Diagrams of strong meson decays: (a) Decay of an S-wave tetraquark meson into two S-wave  $q\bar{q}$ -mesons; (b) Conventional decay of a  $q\bar{q}$ -meson into two  $q\bar{q}$ -mesons; (c) Decay of an S-wave  $J^{PC} = 2^{++}$  tetraquark meson into two S-wave  $q\bar{q}$ -mesons, in a relative D wave; (d) Decay of an S-wave tetraquark meson initially into two color octets and subsequently corrected by a gluon exchange to neutralize the colour[13].

like the conventional (b), but due to not requiring the creation of an additional quark-antiquark-pair OZI-superalowed (a). Thereby any tetraquark state can be written as a linear superposition colour singlet of two coupling  $q\bar{q}$ -states with same total spin, flavour and colour. The amplitude for a particular decay channel is determined by the recoupling coefficients, weighting the terms in the sum. The superallowed decays are accompanied by a broad width of the tetraquark states. The width, making up for a substantial fraction of the tetraquark mass, can explain their experimental elusiveness and the difficulty of allocating clear resonances. Therefore results with similar accuracy as in the conventional baryon- and meson-spectroscopy should not be expected. Because of the necessity for additional gluons to form two colour singlet final states, decays shown in (c) and (d) are suppressed.

### 2.3 The $a_0(980)$ and $a_2(1320)$

Some of the properties of the  $a_0(980)$  and  $a_2(1320)$  meson can already be extracted from previous sections, other important ones, like decay modes and decay widths are summarized in table 2.2. Like Jaffe predicted (section 2.2.3) the experimentally measured decay widths of both isovector states are broad compared to conventional  $q\bar{q}$ -mesons. The  $a_0(980)$  mass and width parameters are strongly distorted, determination of true coupling constants is possible only by a coupled-channel model with energy-dependent widths and mass shift contributions[19].

**Photoproduction** Photoproduction implies the production of a particle using a photon. The production mechanism at the BGOOD experiment additionally includes a proton target, the production scheme in s- and u-channel is shown in figure 2.7. The t-channel in first order is excluded since the  $a_0(980)/a_2(1320)$  do not posses charge or isospin and can not couple to proton or photon. Isospin configuration of the proton and both resonances allows for  $N^*$  and  $\Delta$  as a possible intermediate state.

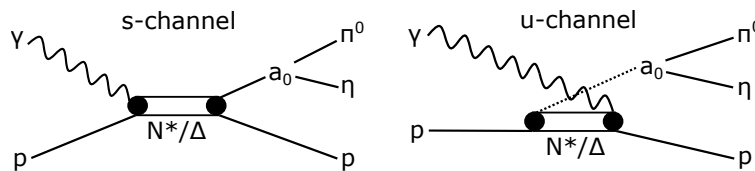


Figure 2.7: Production scheme of the  $a_0(980)$  at the BGOOD experiminet in s- and u-channel.

The threshold energy for photoproduction of both resonances can be calculated precisely. Because of the BGOOD experiment being a fixed target experiment, one can assume the proton target is at rest. The corresponding centre of mass energy or invariant mass energy of the initial state is defined by the relation:

$$\sqrt{s} = \sqrt{(p_\gamma^\mu + p_p^\mu)^2} = \sqrt{2E_\gamma m_p + m_p^2} \quad \text{with:} \quad \begin{aligned} p_\gamma^\mu &= (E_\gamma, \mathbf{p}_\gamma) \\ p_p^\mu &= (m_p, 0) \end{aligned} \quad (2.9)$$

Here  $p_\gamma^\mu$  and  $p_p^\mu$  represent the four-vectors of the photon and the proton composed of their energy  $E$  and momentum  $\mathbf{p}$  information. The necessary beam energy for production of the resonances with mass  $m_{a_0/a_2}$  can be written as:

$$E_\gamma = \frac{s - m_p^2}{2m_p} \quad \text{with:} \quad s = (m_p + m_{a_0/a_2})^2 \quad (2.10)$$

By this calculation one expects the  $a_0(980)$  to be produced at a threshold of  $E_\gamma = 1\,491$  MeV, whereas the  $a_0(1320)$  should be produced at  $E_\gamma = 2\,241$  MeV. In reality these values can deviate slightly to lower energies, due to the widths of the resonances, but they can be used as a approximate orientation.

| Particle    | $I^G(J^{PC})$ | Decay mode      | Fraction ( $\Gamma_i/\Gamma$ ) | Decay width                     |
|-------------|---------------|-----------------|--------------------------------|---------------------------------|
| $a_0(980)$  | $1^-(0^{++})$ | $\eta\pi$       | seen                           | 50–100 MeV (estimate)           |
|             |               | $K\bar{K}$      | seen                           |                                 |
|             |               | $\rho\pi$       | not seen                       |                                 |
|             |               | $\gamma\gamma$  | seen                           |                                 |
| $a_2(1320)$ | $1^-(2^{++})$ | $3\pi$          | $(70.2 \pm 2.7)\%$             | $105.0^{+1.7}_{-1.9}$ (average) |
|             |               | $\rho(770)\pi$  |                                |                                 |
|             |               | $f_2(1270)\pi$  |                                |                                 |
|             |               | $\rho(1450)\pi$ |                                |                                 |
|             |               | $\eta\pi$       | $(14.5 \pm 1.2)\%$             | $113.4 \pm 1.3$ (average)       |
|             |               | $\omega\pi\pi$  | $(10.6 \pm 3.2)\%$             |                                 |
|             |               | $K\bar{K}$      | $(4.9 \pm 0.8)\%$              | $109.8 \pm 2.4$ (average)       |

Table 2.2: Properties of the  $a_0(980)$  and  $a_2(1320)$  resonances[8]

# The BGOOD Experiment

---

The BGOOD experiment located at ELSA<sup>1</sup> facility at the Rheinische Friedrich-Wilhelms-Universität Bonn is a fixed-target experiment in the framework of an international collaboration. It's main purpose is the systematic investigation of baryon resonances non-strange and strange meson photoproduction, especially processes at low momentum transfer to the residual hadronic system. The experiment setup was chosen such that it complements experiments such as Crystal Barrel, Crystal Ball or CLAS. The essential components of the experiment, the central electromagnetic calorimeter made out of bismuth germanate oxide crystals and the forward spectrometer using an open dipole magnet, providing an almost full angular coverage for tracking charged particles as well as high energy-resolution photon detection. In the following sections the technical components of the experimental framework are elucidated, mainly based on the European Physical Journal article about the BGOOD setup[6].

## 3.1 ELSA

The photon beam required for the photoproduction of particles at the BGOOD experiment is produced via coherent bremsstrahlung using an electron beam provided by the ELSA accelerator. The setup is shown in fig. 3.1. The accelerator consists of three stages beam, the LINACs<sup>2</sup>, the booster synchrotron and the stretcher ring, ascending in order in terms of beam energy. Currents in the range of nA can be periodically transferred to the experimental setup every few seconds via slow resonance extraction from the storage ring. The beam energy can be varied up to a maximum of 3.2 GeV while keeping a high duty cycle.

### 3.1.1 LINACs

The first stage comprises two LINACs, using electrons initially gained either from an unpolarized thermionic source or a spin polarized source. The spin originates from irradiating a strained-layer superlattice photocathode with circularly polarized laser light from a flashlamp pumped titan-saphir-laser. Unpolarised electrons are injected into LINAC 1, providing beam energies of 20 MeV, where as the polarized electrons are accelerated in LINAC 2, reaching beam energies up to 26 MeV.

---

<sup>1</sup> Electron Stretcher Accelerator

<sup>2</sup> Linear Accelerators

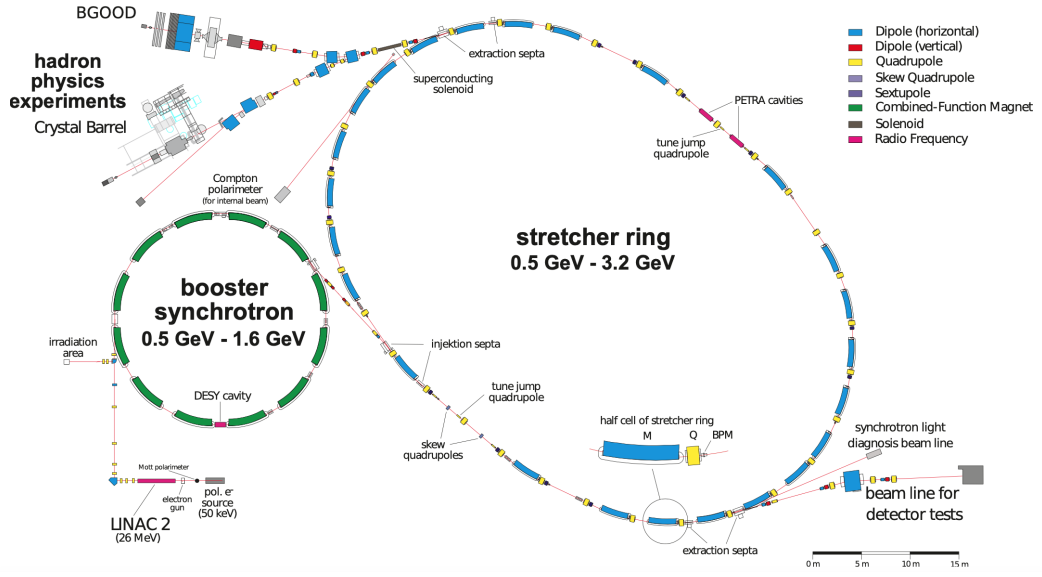


Figure 3.1: Schematic representation of the ELSA accelerator setup, supplying either an area for detector tests (bottom right) or one of the hadron physics experiments (top left), Crystal Barrel and BGOOD with an electron beam[6].

### 3.1.2 Booster Synchrotron

The second stage consists of the fast cycling booster synchrotron with a 69.9 m circumference. Combined-function-magnets constrain the electrons to the circular path with a fixed cycle time of 20 ms leading to a 50 Hz repetition rate. A maximum energy of 1.6 GeV can be reached, but on regular base the beam is extracted at 1.2 GeV. The synchrotron operates with a pulsed beam. The transfer into the third stage, the stretcher ring, is done within one revolution corresponding to injection periods of 0.45  $\mu$ s or 0.8 turns of the stretcher ring[20].

### 3.1.3 Stretcher Ring

Electrons are accumulated over several injections from the booster synchrotron and stored in the stretcher ring with a circumference of 164.4 m until it is homogeneously filled. Depending on the operation mode an internal beam current of multiple mA can be stored, for hadron physics experiments commonly 20 to 25 mA. Once the injection phase stopped further acceleration of the electrons up to 3.2 GeV is achieved by using a fast energy ramp with up to 6 GeV/s[21]. At this point the energy loss due to synchrotron radiation becomes a strong factor and exceeds several hundred keV. A precise guidance of the beam path is accomplished by the repeating combination of a horizontally focusing, magnetic quadrupole field and vertically focusing, horizontally defocussing, magnetic quadrupole field, each respectively followed by open drift space, frequently containing beam bending dipole magnets. One iteration is referred as a FODO<sup>3</sup> cell or stretcher ring cell.

<sup>3</sup> Focussing quadrupole, Open drift space, Defocussing quadrupole, Open drift space

As soon as the requested beam energy is reached slow resonance extraction provides an external electron beam with currents between 0.5 to 1.0 nA for the BGOOD experiment, the beam line from ELSA to the experimental area is shown in figure 3.2 in detail. The extraction phase length of 4 to 15 s with a 1.5 to 2 s pause interval ensures macroscopic duty factors between 70% and 90% (theoretically an unlimited extraction phase is possible as well, leading to a duty factor of 100%). Due to the beams micro-structure of electron bunches, separated by 2 ns, the duty factor is lowered slightly[6] [20].

The polarization of the electrons during the acceleration process is preserved as well as possible. Depolarization effects, caused by resonant coupling of the electron spin precession around the vertical fields of the bending magnets with any component of the accelerator's periodic horizontal magnetic field distribution have been successfully minimized. The maximum achievable polarisation measured at the CBELSA/TAPS experiment, also located at ELSA, was increased to  $(71 \pm 1)\%$  at 2.35 GeV and  $(62 \pm 2)\%$  at 2.92 GeV[21].

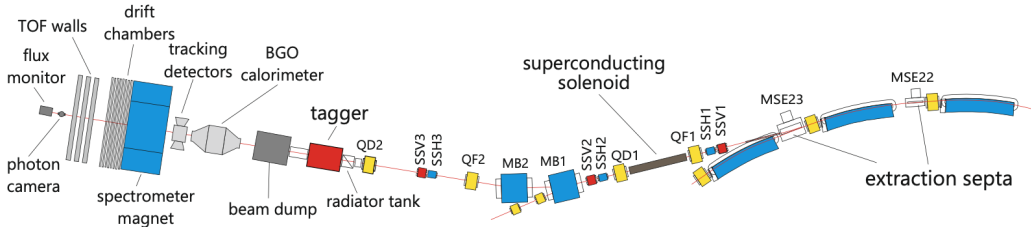


Figure 3.2: The dipole magnets MB1 and MB2 deflect the beam to the BGOOD experiment. Beam position can be adjusted using horizontal and vertical steering magnets, the focus is set by quadrupole magnets. Further accuracy of the photon beam at the expense of the yield can be achieved by using a collimator[6].

## 3.2 BGOOD

The BGOOD experiment is shown in figure 3.3. Its three major parts, the tagger-system, the central detector and the forward spectrometer suit the requirements for investigation of tetraquark and pentaquark states with its special kinematic conditions. The components are further elucidated in this section.

### 3.2.1 Tagger-System

The tagger-system converts the ELSA electron beam into a continuous bremsstrahlung photon beam while simultaneously measuring its energy event wise. Consequently to the spectrum being continuous, the energy and time information of the produced photons are unknown. The tagger system, shown in figure 3.4, operates as a magnet spectrometer that analyses the energy of post-bremsstrahlung electrons  $E_{e^-}$ . By comparing  $E_{e^-}$  to the initial ELSA energy  $E_0$ , the difference can be set as the correlated photon energy  $E_\gamma$ , shown in equation 3.1. The system also defines the production time of the photon, working as a reference point for the hardware triggers. These set the measurement windows for the



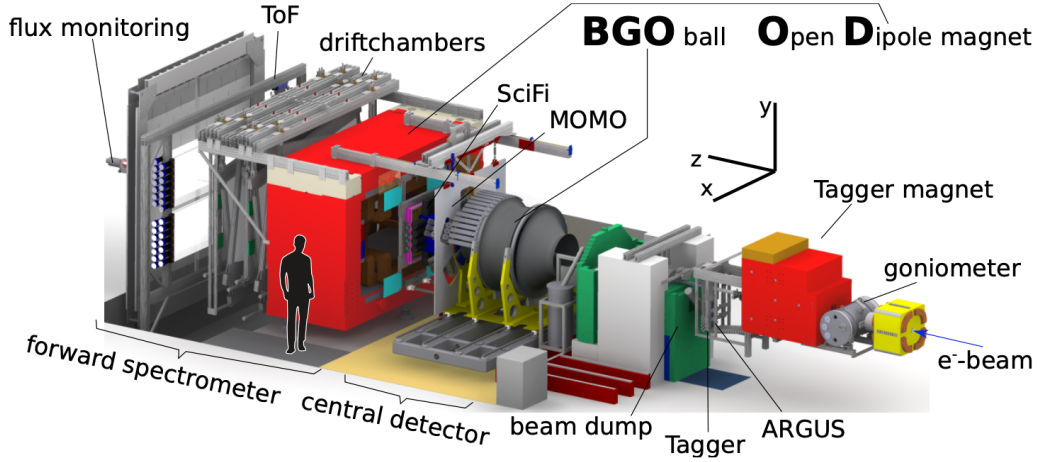


Figure 3.3: Overview over the BGOOD experiment. Specific detector components are shown in detail in the subsequent figures 3.4, 3.6 and 3.8 below. The SciFi detector is not yet marked in the picture[6].

final state particles in central- and forward detector. By looking at the time coincidences from the bremsstrahlung photon particles can be assigned to a corresponding hadronic reaction.

$$E_\gamma = E_0 - E_{e^-} \quad (3.1)$$

**Radiator** The radiator is the component where the bremsstrahlung process takes place. Within the vacuum of the surrounding goniometer system a photon beam is produced by the deceleration of the ELSA electrons, deflected in the Coulomb field of the charged nuclei from the radiator material. The type of photon polarisation depends on the radiator and can be varied. Unpolarized photons are produced by amorphous radiators (copper, capton, ...) of different thickness, while the production of linearly polarized photons requires the diamond radiator, due to its crystalline structure. If aligned correctly by the goniometer system the recoil momentum is distributed over a full row of the crystal lattice, increasing the production on a plane, resulting in a linear polarization of the photons. The output spectrum of the diamond radiator is a mixture of the incoherent process and the coherent one and can be normalized by the spectra of the amorphous radiators. The chromox radiator is used for position and shape determination of the beam profile.

**Tagger Magnet** The trajectory of the photon and the associated post-bremsstrahlung electron diverge when entering the tagger dipole magnet. The electron path is bent by the Lorentz force towards the tagger hodoscope based on its remaining momentum  $p_{e^-}$  and the integrated magnetic field strength  $\int B \cdot dl$ . Electrons not participating in the bremsstrahlung process, thus keeping their initial energy, are deflected in an angle of  $7.74^\circ$  for a  $B/E_0 = 0.43 \text{ T/GeV}$  ratio, corresponding to a magnetic field value of 1.376 T. This angle is responsible for the positioning of the read out detectors and the beam dump, where electrons not contributing to the photon beam are stopped. The magnet is capable of producing even higher magnetic field values up to 2 T, but is kept in a range where the deviation from a linear behaviour with respect to the applied current is less than 1% [6][22].



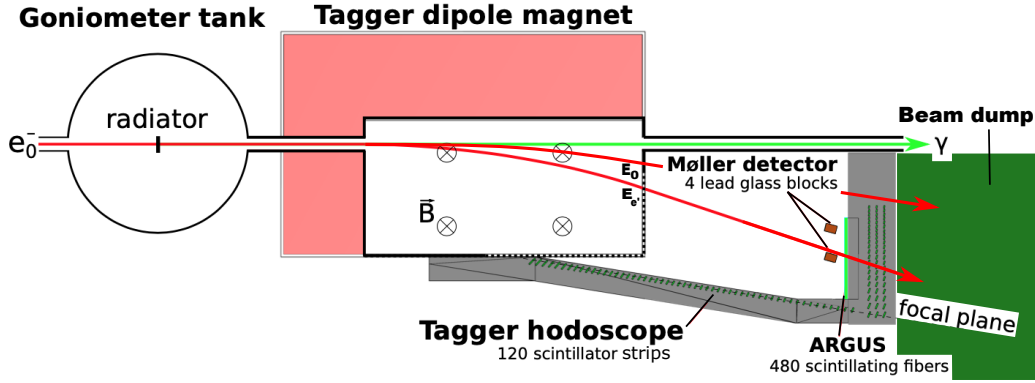


Figure 3.4: Side view of the BGOOD tagging system. The trajectory of the electrons are bent by the dipole magnet, while the photons follow the beam line. Electrons not participating in the bremsstrahlung process (upper red line) miss the scintillators (small green rectangles). They are stopped by the beam dump[23].

**Tagger Hodoscope** The tagger hodoscope design results from its spacial limitation by the beam dumb and the restriction to 120 scintillators by the number of available high voltage channels. There are 54 scintillators placed in the focal plane, while 66 are placed in a vertical construction, measuring the energy of the post-bremsstrahlung electrons. The gap between the bent primary electron beam and the middle of the nearest scintillator is minimized to about 2 cm, increasing the corresponding covered tagging range to  $(10 \div 90)\%$  of  $E_0$ . To assure the hit of an electron the scintillators are arranged with an overlap of 55% and coincident signals of two PMTs<sup>4</sup> are requested. In the vertical tagger component, this is implemented by stacking up at least three scintillators in one plane. The resolution can be defined as the width of the overlapping areas, causing the scintillator width to decrease towards the direction of less deflected electrons, whose tracks narrow. Nevertheless the energy width changes at four different positions in the vertical hodoscope component:

| Hodscope Component | Horizontal | Vertical  | Vertical  | Vertical  | Vertical  |
|--------------------|------------|-----------|-----------|-----------|-----------|
| $E_{\text{width}}$ | 10 MeV     | 15 MeV    | 20 MeV    | 30 MeV    | 40 MeV    |
| $E_{e^-}$          | 1 030 MeV  | 1 570 MeV | 2 130 MeV | 2 580 MeV | 3 200 MeV |

Table 3.1: Energy bin width and the upper electron energy threshold (scaled for 3.2 GeV from[24]).

This behaviour leads to a percentage energy resolution that varies from 0.4% to 1.7% of  $E_0$ , depending on the electron energy. Additional to the specialities of the scintillator arrangement, the use of different PMTs, the Hamamatsu R7400U with smaller diameter and lower transit time at the vertical hodoscope component is necessary to manage the higher rates from low energetic bremsstrahlung production. For the horizontal component ET Enterprise 9100SB PMTs are installed. Both achieve time resolutions of approximately 200 ps[22][24].

**ARGUS detector** The ARGUS scintillating fibre detector complements the vertical component of the tagger hodoscope in the region of 30% to 66% of the incoming ELSA electron energy. The main

<sup>4</sup> Photomultiplier tubes

purpose is a more precise approximation of the electron position, resulting in an improved energy resolution. The 480 double-clad BCF-10 scintillating fibres are arranged in three layers. With its diameter of 2 mm each fibre covers a smaller area than the underlying tagger scintillators. By setting a spatial coincidence of electron trajectory between ARGUS and the hodoscope as a condition, the energy resolution can be increased to 0.08% to 0.45% of  $E_0$ , this also helps for better determination of the degree of polarization. Nevertheless, both parts are indispensable, in terms of time resolution, ARGUS can not compete with the hodoscope[25][26].

**Collimators and cleaning magnet** The tagging system closes with a permanent magnet in between a set of lead collimator with a length of 20 cm. The first collimators with an inner diameter of 7 mm reduces the incoherent contribution in the bremsstrahlung spectrum, leading to an enhancement in the degree of polarisation. Unfortunately, the collimation causes the production of electron-positron pairs. However, these can be removed by the combination of the magnet, filtering the photon beam from lower energetic charged particles, and the other collimator with a wider diameter of 12 mm, to stop high energetic charged particles for which the magnet is not sufficient.

**Flux monitoring with FluMo and GIM** Closely related to the tagger-system and therefore explained in this subsection are the detectors for flux monitoring, GIM<sup>5</sup> and FluMo<sup>6</sup>. They are placed at the very back of the BGOOD experiment more than 7 m downstream from the target. In combination with the tagger-system GIM and FluMo determine the efficiency  $P_\gamma(E)$  for bremsstrahlung photon to reach the target, allowing to define the collimated photon flux present at the target. A more detailed explanation is given in the PhD thesis of Georg Scheluchin[23]. The flux is required to perform normalizations, exemplary in cross section measurements.

To evade the difficulty of measuring photons at high intensity with one detector, this task is split up to the two detectors. The GIM detector is a fully absorbing lead glass detector with dimensions of 14 cm × 14 cm × 28 cm. Incoming photons are measured by detecting Cherenkov light pulses, that are relatively short compared to scintillation light, which is crucial for high rate stability. The detection efficiency relies on read out electronics (Hamamatsu R2083) affected by dead time effects and the detector is sensitive to radiation damage and can not be kept in the beamline continuously. In contrast this is possible for the FluMo detector, consisting of 5 small plastic scintillation detectors with geometry of 5 cm × 5 cm × 0.5 cm. As shown in fig. 3.5 these respond well to  $e^+e^-$  pairs, produced by the photon beam in the open space between the dipole magnet and the detector, whereas photons will be detected with low efficiency. By determining the ratio of  $e^+e^-$  pairs, that is proportional to the photons counts in the GIM at low intensity, the flux can be estimated at higher intensities just from the FluMo detector.

### 3.2.2 Central detector

The central detection system, shown in fig. 3.6, contains and encloses the cryogenic liquid hydrogen  $H_2$  or deuterium  $D_2$  target cell. It detects particles in a polar angle range of  $(25 \div 155)^\circ$ . The BGO

---

<sup>5</sup> Gamma Intensity Monitor

<sup>6</sup> Flux Monitor

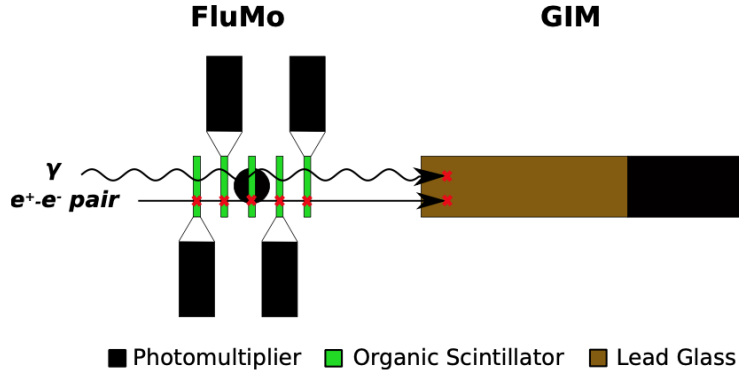


Figure 3.5: Overview of the arrangement of the FluMo and GIM detector in a reference measurement[23].

rugby ball is supported by two MWPCs<sup>7</sup> and a scintillator barrel for charge recognition and tracking.

**Target** The target cell is a 4 cm diameter aluminum cylinder, enclosed by 0.1 mm thin Mylar foil windows at beam entrance and exit. It is contained in a vacuum pipe along the beam axis in the center of the central detector system and connected to the beam pipe by a fast closing valve, which guarantees the thermal insulation. The hydrogen/deuterium cooling works with a cryogenerator system initially cooling down high purity helium gas via two Gifford-McMahon cycles varying the pressure isothermally from 17 bar down to 5 bar. Subsequently, the target gas is cooled down by the helium to working temperature of about 17 K and 22 K respectively, through heat exchangers and liquefies inside the cell[27]. To avoid freezing inside the target cell the temperature is constantly monitored by three probes (one connected with a security system) and stabilized by a heating resistor. To fulfill different experimental requirements cells with an effective length (the Mylar foil expand outwards due to the pressure difference) of 6.1 cm and 11.1 cm can be utilized[23]. The smaller one offers a target area density of  $0.425 \text{ g cm}^{-2}$  corresponding to  $2.58 \times 10^{-7} \mu\text{b}^{-1}$ .

**MWPCs** Starting from the reaction point the first detector layers are the an inner and outer MWPC, constructed identically in a coaxial cylindrical configuration. Charged particles crossing the chambers are tracked by ionizing a gas mixture of 69.5% argon, 30.0% ethane, and 0.5% halocarbon 14 ( $\text{CF}_4$ ). By their acceleration inside the electric field, the emerging electrons cause a localised cascade near the  $20 \mu\text{m}$  diameter gold-plated tungsten anode wires stretched along the longitudinal axis. Copper strips of thickness  $0.1 \mu\text{m}$ , width 4.5 mm and a separation of 0.5 mm, working as the cathode at an operational voltage of 2 500 V. It should be noted, that the inner and outer strips, laminated to the interior surfaces of the in  $50 \mu\text{m}$  Kapton film covered 2 mm thick Rohacell walls are tilted by  $\pm 45^\circ$  with respect to the anode alignment. This leads to unambiguously distinguishable intersection points of anode and cathode and allows for position reconstruction with only one chamber. Combined information from both chambers consequently provide the absolute track. Resolutions differs from  $\delta z \simeq 500 \mu\text{m}$  along the beam axis to  $\delta\phi \simeq 1.5^\circ$  in azimuthal and  $\delta\theta \simeq 1^\circ$  in polar angle[6]. As shown in figure 3.6 the polar angular coverage of  $(8 \div 163)^\circ$  is slightly bigger than the one of the other central

<sup>7</sup> Multi wire proportional chamber

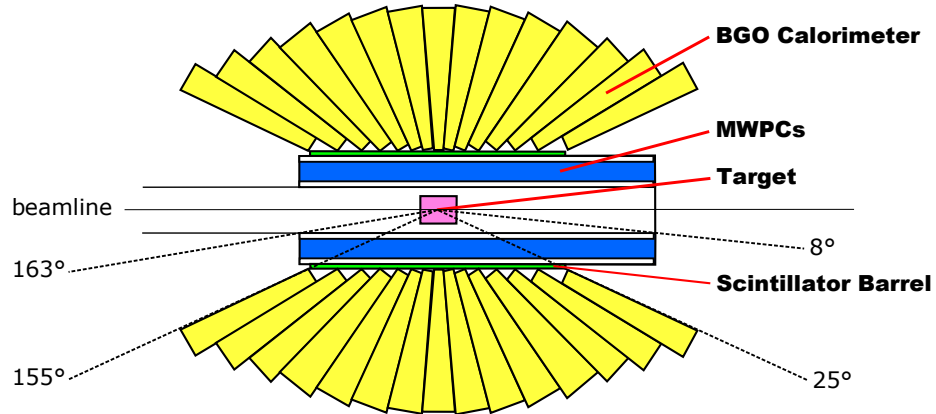


Figure 3.6: BGO central detector system, photon beam direction is from left to right. The SciRi detector, mounted inside the forward opening cone of the BGO calorimeter, is missing.

detector parts and partly overlaps with the range of the intermediate and forward detector system. The angles from  $8^\circ$  to  $18^\circ$  are shadowed by plastic flanges (almost negligible for neutral particles[28]), attached for mechanical stability.

**Scintillator barrel** The scintillator barrel consists of 32 plastic scintillator bars arranged in a cylinder of length 43 cm and radius 9.75 cm. It is placed between the MWPC and the BGO calorimeter with the intention of performing an energy loss measurement  $-dE/dx$ . The deposited energy is only a fraction of the total energy, however, it can be further interpreted as an indication for a charged particle. The detection efficiency for charged particles is  $\approx 98\%$ , whereas photon and neutron detection efficiencies are  $< 1\%$ . The polar angle range of the scintillator barrel matches the one of the BGO calorimeter, discussed in the paragraph below. The azimuthal angular coverage of one scintillator bar matches exactly the azimuthal angular coverage of one BGO crystal.

**BGO calorimeter** The outermost and main detector layer of the central detector system is the BGO calorimeter formerly installed in the GrAAL experiment to measure energy and direction and time of particles. As the name states, the calorimeter consist of 480 bismuth germanium oxide crystals, due to their high energy resolution and short radiation length of  $X_0 = 1.118$  cm[29]. Thus, the crystal depth of 24 cm is equivalent to over 21 radiation lengths. The detector geometry features 15 crystal sectors in polar angle covering  $\Delta\theta = (6 \div 10)^\circ$  individually and a combined range of  $(25 \div 155)^\circ$ , whereas each 32 crystals form a ring in azimuthal angle, corresponding to  $\Delta\phi = 11.25^\circ$  per crystal. This structure requires eight different dimensions of the crystal design shaped as pyramidal sectors with trapezoidal basis to achieve a constant thickness for all particles emitted from the target point. Stability is given by the enclosing basket structure where each basket consists of 20 individual cells made of carbon fibre. Precise light readout, supported by the crystals being wrapped in  $30\mu\text{m}$  aluminised Mylar foil, is done via photomultiplier tubes (linearity selected Hamamatsu R580 or R329-02). Aside from an iron cover in the forward hemisphere, shielding the entire central detector and its read out electronics from the fringe field of the Open Dipole magnet (3 mT at the most downstream end), these PMTs are additionally protected with  $\mu$ -metal. Signals of the PMTs are handled by Wiener AVM16

sampling ADCs with a sampling rate of 160 MHz. The time resolution of 2 ns is superior compared to the MWPCs and the scintillator barrel, therefore, time information is expanded to all central detector components.

The BGO calorimeter is optimized for photon detection. Energy deposition of the entire photon energy is performed by creating an electromagnetic shower via alternating processes of pair production and bremsstrahlung. In contrast, heavy charged particles deposit only a small part of their energy by ionization according to the Bethe-Bloch formula, making them harder to detect. The BGO calorimeter response reliably to protons at low kinetic energies, the ones above  $p_T > 450$  MeV escape the detector[30]. Further pions, neutrons and deuterons can be identified with sufficient efficiency.

### 3.2.3 Intermediate detector

To cover the acceptance gap between the central- and the forward detector system a scintillating ring detector (SciRi) is installed for direction reconstruction of charged particles. Time-of-flight measurements with high detection efficiency, better angular- and time resolution should be provided by multi-gap resistive plate chambers (MRPC), originally built for the ALICE<sup>8</sup> experiment but are not operational yet.

**SciRi** The scintillating ring detector, mounted inside the forward opening cone of the BGO calorimeter as shown in fig. 3.8, consists of 96 plastic scintillators with a thickness of 20 mm. The scintillators are arranged in 3 sections of  $\Delta\theta = 5^\circ$  in the polar angle intermediate range of  $(10 \div 25)^\circ$ , leading to exactly 32 segments in azimuthal angle, which match the division of the BGO calorimeter. The read out is done individually by Hamamatsu S11048(X3) avalanche photo diodes (APDs). Time resolutions of approximately 3 ns can be achieved.

### 3.2.4 Forward detector

The Lorentz boost causes the final state particles of a fixed target experiment to be created in a more forward direction along the beam axis, therefore, the BGOOD forward spectrometer, shown in fig. 3.8, covers the angles from  $(1.5 \div 12)^\circ$ . Here particle identification works by tracking the charged particles in front of the open dipole magnet by two scintillating fibre detectors, MOMO and SciFi, and afterwards through eight double layers of drift chamber. The curvature of the particle trajectory combined with information from the velocity measurement from three layers of scintillator ToF<sup>9</sup> lead particle identification.

**MOMO and SciFi** MOMO and SciFi are both similar operating scintillating fibre detectors with a slightly different fibre configuration. The 672 fibres of MOMO, with a diameter of 2.5 mm, are arranged in three layers with an angle of  $60^\circ$  between each adjacent layers. One layer consist of two planes complementing themselves by filling the gap between fibres of one plane with own fibres of the other plane. This causes charged particles to pass either one or two fibres per layer. Position measurement then requires coincidence hits within 20 ns between either two or three of the layers.

<sup>8</sup> A Large Ion Collider Experiment

<sup>9</sup> Time-of-Flight-walls

With this circle like design MOMO covers a diameter of 44 cm with a central 4.5 cm hole for the photon beam to pass. The SciFi detector is rectangular shaped covering 66 cm in width and 55 cm in height and leaving a square hole of  $16\text{ cm}^2$  in the centre. Its 640 fibres of 3 mm diameter are divided into two layers aligned in a  $90^\circ$  angle. Separation of 1 mm between the fibres of each layer guaranty the passing of one or two fibres per layer for a charged particle, combined information of both layers determines the particle position. The good time resolution of the fibres allows for a tight time cut of 20 ns between adjacent fibres. Like in the central detector the read out photomultiplier tubes, Hamamatsu R4760 and Hamamatsu H6568 need to be shielded against the dipole magnets fringe field using Permenorm and  $\mu$ -metal respectively.

Particle position reconstruction efficiency, determined by the comparison of real and simulated data, is noticeably worse for MOMO with 80% than for SciFi with 97.5%. This is caused by MOMO being originally built and optimized for the larger particle penetration angles at COSY whereas at the BGOOD experiment the angles are smaller inducing a larger fraction of fibre edge hits. If MOMO does not respond to a particle, the trajectory prior to the magnetic field is defined by only using the centre of the target and the SciFi detector.

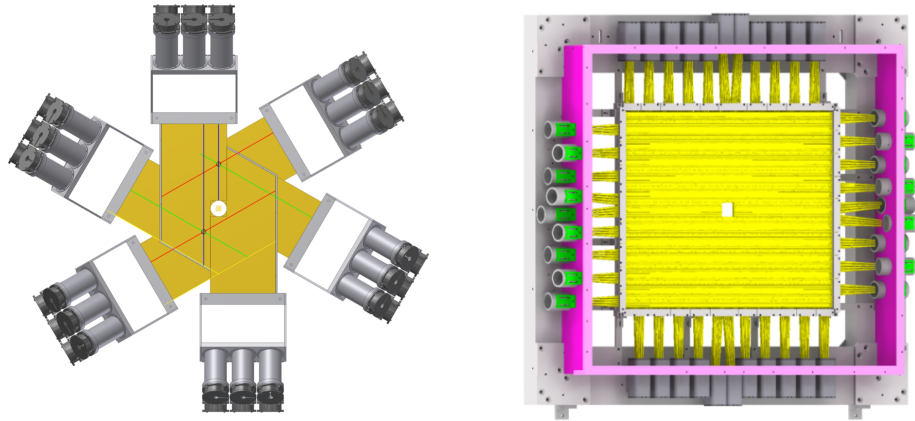


Figure 3.7: Schematics of MOMO (left) and SciFi (right). The coloured lines indicate how the information different layers of MOMO is combined in the reconstruction process of the particle impact points in case of multiple hits.

**Open dipole magnet** The open dipole magnet is the essential component of the forward spectrometer, creating the magnetic field for the determination of the charge and deflection of the particle trajectory, that is evaluated by the other detectors. The outer dimensions are 280 cm (height)  $\times$  390 cm (width)  $\times$  150 cm (length), with inner dimensions of 54 cm (height)  $\times$  84 cm (width) for particles and the beam to pass through. In terms of angle this corresponds to an acceptance up to  $12.1^\circ$  and  $8.2^\circ$  in horizontal and vertical direction, respectively. The maximum achievable integrated field at a current of 1 340 A is approximately 0.71 T m. Apart from the gap the field up- and downstream of the magnet is described by a three dimensional field map, so that particle momentum can be measured accurately and its influence on nearby detector components can be taken into account.



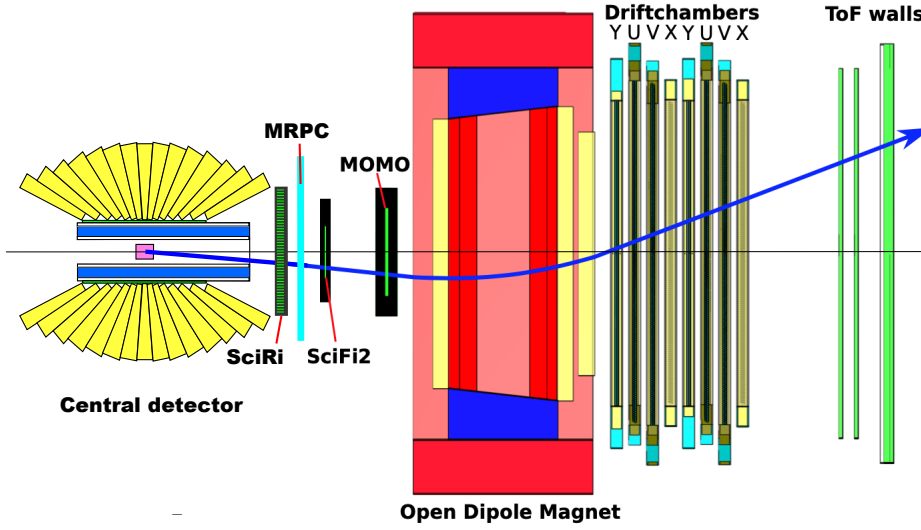


Figure 3.8: Top view of the BGO-OD experiment with the blue line representing the trajectory of a charged particle in the magnetic field of the open dipole magnet. The letters X, Y, U and V display the different fibre orientation inside the drift chamber, explained in paragraph 3.2.4. Adapted from [23].

**Drift chambers** Charged particle tracking downstream of the dipole magnet is performed by eight double layer drift chambers, covering a sensitive area of  $246 \text{ cm} \times 123 \text{ cm}$ . For precise track reconstruction the wire orientation of the chambers varies as shown in fig. 3.8 between horizontal (X), vertical (Y) and slightly rotated by  $\pm 9^\circ$  (U and V) with respect to the vertical chamber. Dimensions of the single U and V have to be a bit larger to preserve the same total active area. The single drift cells of each chamber have a hexagonal structure with a width of 17 mm, which are arranged in two layers at 15 mm distance to avoid left-right ambiguity. The middle has a  $25 \mu\text{m}$  diameter anode (signal) wire kept on a ground potential surrounded by six cathode wires of the same diameter, typically set at high voltages, and field-forming wires at the edges to assure an equal field distribution and shield against external field distortions. Due to the Drift chambers not having a central hole, signal wires of a  $5 \text{ cm} \times 5 \text{ cm}$  area have been made insensitive by galvanising additional gold to them. The gas mixture of argon (70 %) and  $\text{CO}_2$  (30 %) provides a drift velocity of  $7 \text{ cm}/\mu\text{s}$ , which is not high compared to other gas mixtures, however, the achieved position resolution of  $\delta x < 300 \mu\text{m}$  is more than sufficient for the total spectrometer to achieve a momentum resolution of  $\delta p/p \simeq 3\%$  over a range of approximately 400 to 1 100 MeV/c and a polar angle resolution better than  $1^\circ$ .

**Time-of-flight spectrometer** The time-of-flight spectrometer, consisting of three walls of plastic scintillators segmented into individual horizontally oriented bars, is placed 5.6 m downstream from the target. The larger distance to the target enables a more accurate measurement of  $\beta$  (time information of the tagger is used for the start), but also results in the need for a larger active area, here of  $3 \text{ m} \times 3 \text{ m}$  with horizontal gaps of 10 cm to 22 cm at the center, to avoid the photon beam as well as  $e^+e^-$  pairs abundantly produced in the target and air. The readout is performed with Philips XP2282/B photomultiplier tubes. Time resolutions of  $\sigma = 0.34 \text{ ns}$  is accomplished by minimizing time walk of leading edge discriminators by Time over Threshold (ToT) technique.

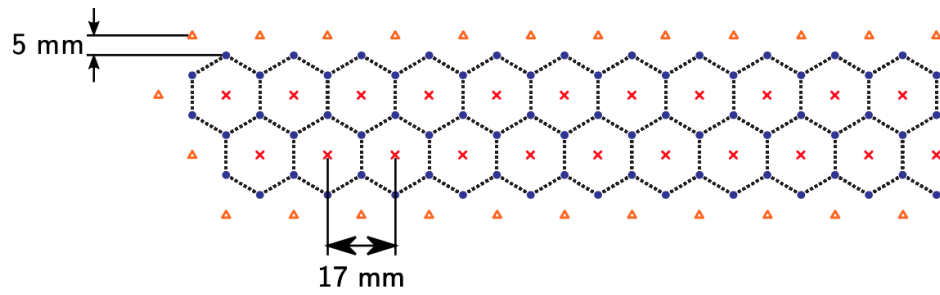


Figure 3.9: Arrangement of the signal (red crosses), field forming (orange triangles) and potential (blue circles) wires inside each of the drift chambers resulting in the hexagonal drift cell geometry (dashed blue lines).



## Basic methods of particle identification

### 4.1 The EXPLORA framework

Data analysis of the BGOOD experiment operates within the ExPIORA<sup>1</sup> framework, a C++ extension to the ROOT library originally developed by the CBELSA/TAPS collaboration at Bonn. Since a reduced version has been used at the BGOOD experiment in 2011 many fundamental changes have been made, while keeping the plugin-based structure, the underlying programming languages and the strong coupling to ROOT. Typically each of these plugins deal with an individual task of the analysis. They extract the physics information by creating and exchanging specialized objects and are implemented in larger building blocks to form a complete analysis chain, schematically shown in figure 4.1. The chain, common to many event based particle physics experiments, starts with the acquisition

<sup>1</sup> Extended **P**luggable **O**bjectoriented **R**OOT-ified **A**nalysis

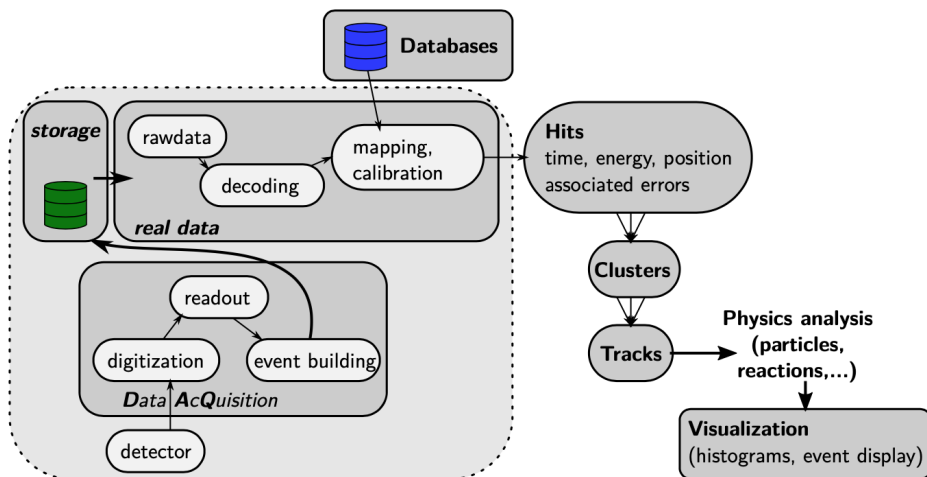


Figure 4.1: Overview of the building blocks used by the ExPIORA framework for event-based data analysis at the BGOOD experiment. Deeper explanation of the structure can be found in the thesis of Oliver Freyermuth [31].

of raw data from the different detectors, combining them to one easy storable event. From there analysis software starts to firstly decode and then map the data by using information about calibration constants and time corrections from the databases. Simultaneously, data of one detector channel with multiple different readout modules is grouped together. The first reconstruction step applies detector geometry and error information to the detector channel and creates a *hit*, if the electrical signal corresponding to the deposited energy exceeds a preset threshold. Multiple hits with close space and time correlation, assumed to be produced by same incident particle within in one detector can be summed into *clusters*. Extending this procedure the clusters of several detectors reproducing the path of the same particle can be further combined to complete a *track* (if there is a single clusters the tracks can be defined by taking the position of the target into account). In the following sections the methods of the cluster- and track building process for central and forward spectrometer by applying basic selection cuts on time, energy and other properties are explained in more detail. The tracks provide a favourable starting point for further analysis. They reconstruct the corresponding particles and can be combined to identify a reaction candidate.

Beside the raw data from real BGOOD beam times, ExPIORA can also operate with simulated data, acquired in two steps. First reaction kinematics, as well as first generation particles including a post-bremsstrahlung electron and the not yet decayed final-state particles of the reaction, are produced by an event generator. The decay of the particles is then simulated in the second step via Monte Carlo methods, using ExPIORA's information of the BGOOD detector geometry and magnetic fields. Energy deposition in the detectors is provided by the Geant4<sup>2</sup>[32], a toolkit for Monte-Carlo method replicating a particles passage through matter.

## 4.2 Track building at BGOOD

Due to the specificity of the different BGOOD detectors, measuring different physical quantities, the track types do not have the same parameters. Table 4.1 explains the track parameters of each detector segment. However, common ground for the tagger-, central- and intermediate tracks are selection cuts on the time coincidence with respect to the event trigger. The time distributions are shown in figure 4.4. These are already adjusted by the subtraction of the offset, that results from the travelled distances between the bremsstrahlung event, the associated hadron event and the respective detector. As a result the distributions are centered around zero.

**Tagger tracks** The Tagger tracks combine information of the Tagger and the ARGUS detector to provide a precise value of the initial photon energy. As stated in section 3.2.1 the ARGUS has a better energy resolution, therefore, in case of temporal coincidence with the Tagger its energy information is preferred in the overlap region. The absolute time information, which works as a reference point for the ToF detectors and consequently has to be very accurate, is always taken from the Tagger. Thus a Tagger cluster is implicitly required. The time distribution with regard to the event trigger is shown in figure 4.4. Events within a  $-1.5$  to  $1.5$  ns range are assumed to be correlated with hadronic events and are selected, the small secondary peaks caused by the pulsed electron bunch structure of the 500 MHz accelerator are removed.

---

<sup>2</sup> Geometry and Tracking 4

| Track type         | Detector                                | Parameter   |
|--------------------|---|---|
| Tagger track       | Tagger<br>ARGUS                         | Initial photon energy   |
| Central track      | Scintillator Barrel<br>BGO Calorimeter  | Energy<br>Position<br>Discrimination of charged and neutral particles |
| Intermediate track | SciRi                                   | Position  |
| Forward track      | MOMO<br>SciFi2<br>Drift chambers<br>ToF | Momentum<br>Direction<br>Charge<br>Time of flight                     |

Table 4.1: Overview of the detectors involved in the track building process and the different parameters of each track type. Additionally, every track type possesses time information correlated to the event trigger[23].

**Central tracks** The central tracks comprise information from the scintillator barrel and the BGO calorimeter. In a first step clusters of the calorimeter are formed, by space and time correlation. These vary for different particle types as illustrated in figure 4.2. While heavy charged particles like protons and  $\pi^\pm$  deposit their energy mostly via Bethe-Bloch ionization within a single crystal, high energetic photons and electrons create a cascade via pair production and bremsstrahlung, which extends over several crystals. The transverse development of such an electromagnetic shower can be calculated by the Molière radius and should completely depend on material properties, namely the critical energy  $E_c$  and the radiation length  $X_0$ . Cluster size, therefore, is expected to be constant over energy. However, each detector segment suppresses low energy signals to remove noise and with higher photon energy more segments surpass the threshold, resulting in an increase of hits per cluster, shown in figure 4.3. The position  $r$  of a photon or electron cluster is determined by all detector segments weighted by the

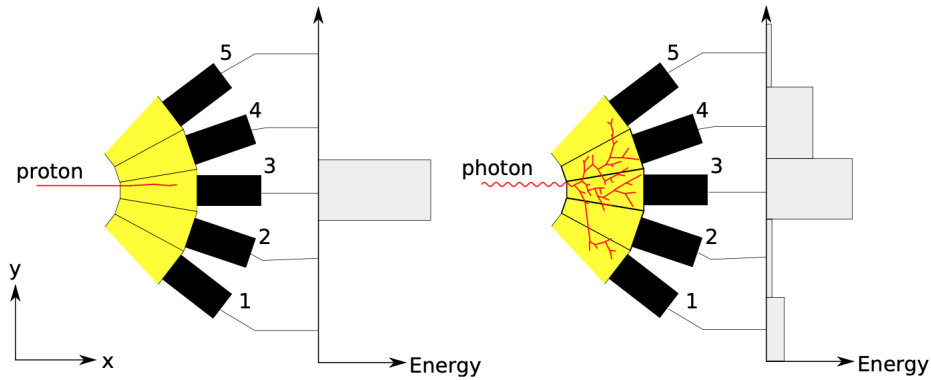


Figure 4.2: Creation of a BGO calorimeter cluster for a proton (left) and a photon (right) with the PMT channel drawn against the measured energy. The allocation of deposited energy, not being distributed perfectly Gaussian for one single photon events due to statistical nature of electromagnetic shower development, can sometimes produce split-off clusters. In this example the crystal number 2 does possibly not exceed the threshold, resulting in two clusters whose energy is not assigned to the same photon[23].

square root of their energies  $E_i$ , resulting in a better angular resolution compared to the heavy charged particles, which position is in most cases attributed to one crystal limited in resolution by the crystal size. It can be written as:

$$r = \frac{\sum_i r_i \sqrt{E_i}}{\sum_i \sqrt{E_i}} \quad (4.1)$$

Time  $t$  and Energy  $E$  of a cluster are defined by the relations:

$$E = \sum_i E_i \quad t = \frac{\sum_i t_i E_i^2}{E_i^2} \quad (4.2)$$

Unification with the scintillator Barrel hits is done in a second step where a comparison in  $\phi$  angle and time is done. The  $\phi$  difference between both detectors, shown in figure 4.3, validate a selection cut of  $-20^\circ$  to  $20^\circ$ . The repeating peak structure in intervals of  $11.25^\circ$  originates from clusters with one hit mentioned above. For further analysis a selection of events in the range of  $-5$  to  $5$  ns, based on the central track time distribution, as shown in figure 4.4, is done.

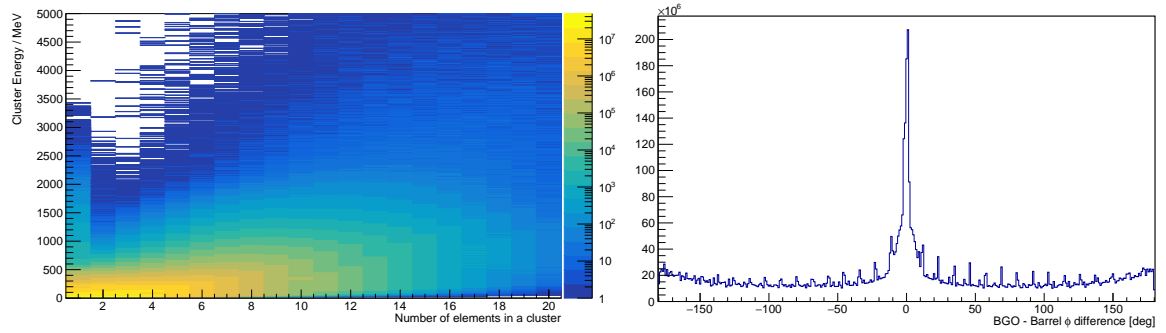


Figure 4.3: The number of hits per cluster in relation to the cluster energy (left) and the angular difference in  $\phi$  between BGO clusters and Barrel hits (right). The vertical line for exactly one hit in the cluster is caused by heavy charged particles and can be clearly identified.

**Intermediate tracks** The intermediate tracks are built only by the SciRi detector, in most cases only a single hit is measured (4% of the particles pass between two scintillators leading to a cluster with two hits). As shown in figure 4.4 the time resolution is far worse than the other tracks, caused by the read out with APDs. A broad selection cut of  $-50$  to  $50$  ns is applied. The APDs are initially designed to work with higher light output from inorganic scintillators, an adjustment to SciRi organic ones is done to provide a higher detection efficiency at the expense of energy resolution. Since the detectors main task is the coverage of the blind region this sacrifice is negligible.

**Forward tracks** The forward tracks are formed by information from MOMO, SciFi2, drift chambers and the ToF walls. In a first step the particle trajectory in front of the dipole magnet is checked, particles not originated from the target are discarded. Afterwards a draft version of the complete

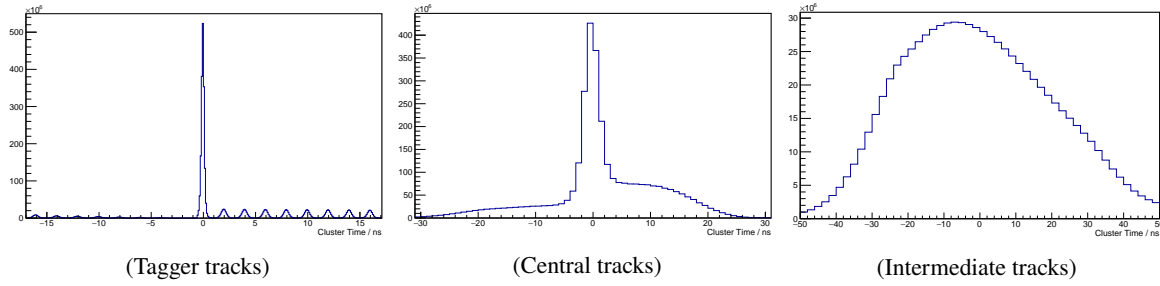


Figure 4.4: Time distributions of tagger-, central- and intermediate tracks correlated to the event trigger. The distributions are adjusted to their relative time offset, i.e. they are centered around zero.

trajectory is made by involving clusters from the ToF walls. A cluster, which is required for proceeding, consist of either one, two or three time and space coincident hits, each from the one of the three separated walls. Here one hit occurs most often due to particles with lower momentum generally being stopped by the first wall. The MOMO and SciFi trajectory is extrapolated to the ToF z-position, the y-difference is used to assign the corresponding clusters. Field non-uniformity and fringe fields are ignored for now. Connecting the extrapolated MOMO and SciFi track, the magnet center and the ToF position make a good estimation of the actual trajectory. The closest drift chamber hits then ensures an even better result, that is refined by a fit including non-uniformity and fringe fields as well as the energy loss due to Bethe-Bloch ionization.

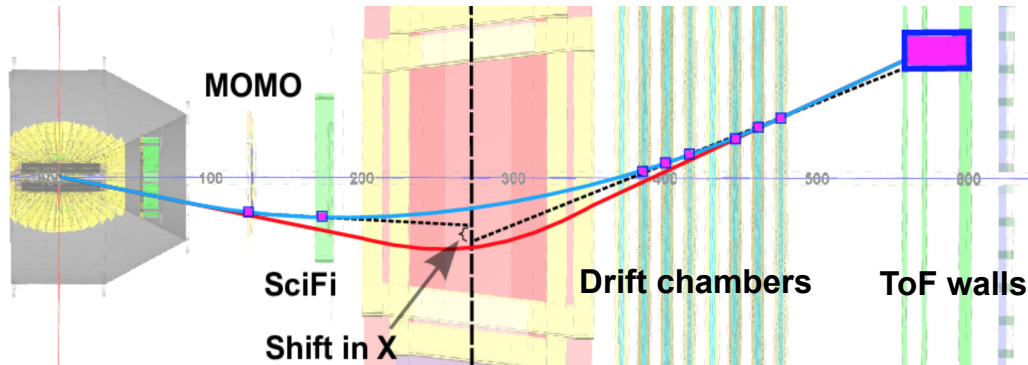


Figure 4.5: Graphical presentation of the track building process. The red line is the first trajectory estimation with a boxlike magnetic field inside the magnet, the gap between extrapolations of the upstream and downstream parts of the trajectory is labelled "Shift in X". The blue line then represents the corrected trajectory.[6].

Beside their use in determination of the trajectory, ToF walls main function is the velocity measurement of a particle, that allows for calculation of momentum and mass. The tagger time is set as a start time, the distance between the ToF wall, the tagger and the target is well known. Because of the long flight times of heavy low energetic particles the acceptance window for one event must be really broad, sometimes causing accidental coincidences with other events. The accidentals are nearly always  $e^{\pm}$  pair production from the beam, triggered by bremsstrahlung electron wrongly selected to set the start time. This results in additional peaks beside the expected  $\beta$ -time correlation, which also transfer into the  $\beta$ -momentum distribution. These can be clearly identified in figure 4.6.

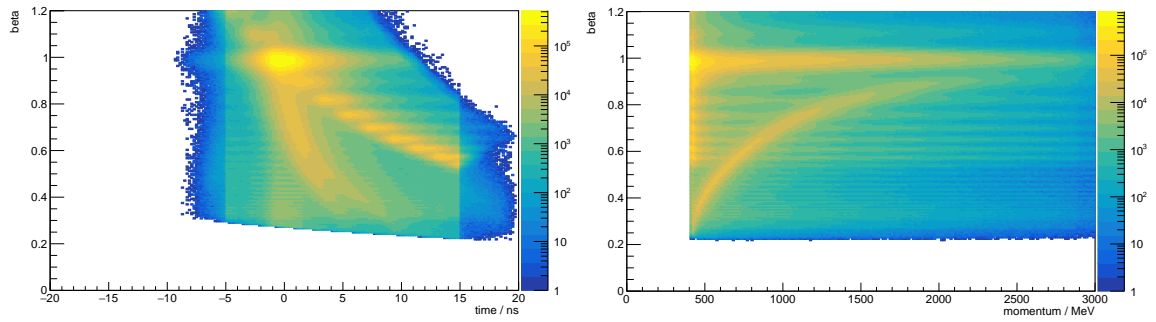


Figure 4.6: Relative particle velocity  $\beta$  against MOMO and SciFi time (left) and momentum (right). The accidental coincidences appear as visible peaks in intervals of approximately 0.2 ns.

To solve this problem independent of the particle type, a two-dimensional selection in the distribution of relative velocity  $\beta$  against time is made. This reduces the accidental coincidences noticeably, the improvement is shown in figure 4.7.

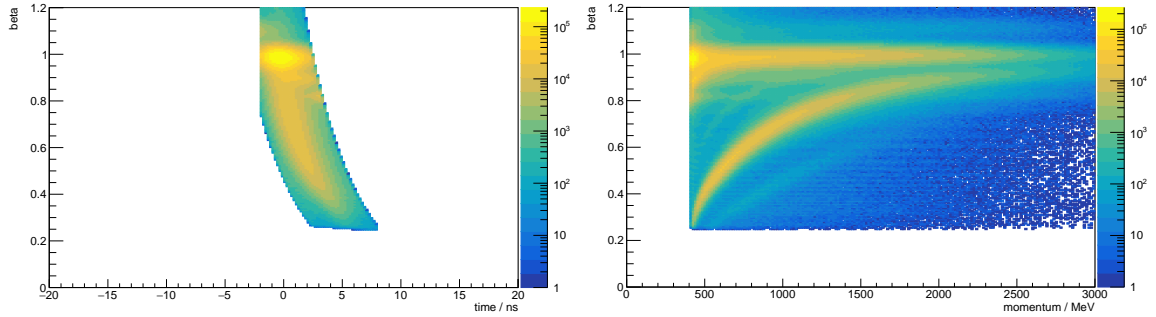


Figure 4.7: Relative particle velocity  $\beta$  against MOMO and SciFi time (left) and momentum (right) with applied selection. The accidental coincidences are reduced significantly. Beside the two dominant lines originated from pions and the heavier protons, now even the small kaon line becomes weakly visible in the middle of the  $\beta$  vs. momentum plot.

## Event selection for the $\gamma p \rightarrow \pi^0 \eta p$ reaction

### 5.1 Identification of the Proton

The first step for the investigation of the  $\gamma p \rightarrow \pi^0 \eta p$  channel is the identification of the proton by the forward spectrometer. Because no other charged particle is expected to be measured for the chosen reaction channel, exactly one positively charged forward track is required along with no particle detection by the SciRi detector in the intermediate region. The distributions of particle numbers for the different detector regions can be seen in figure 5.1.

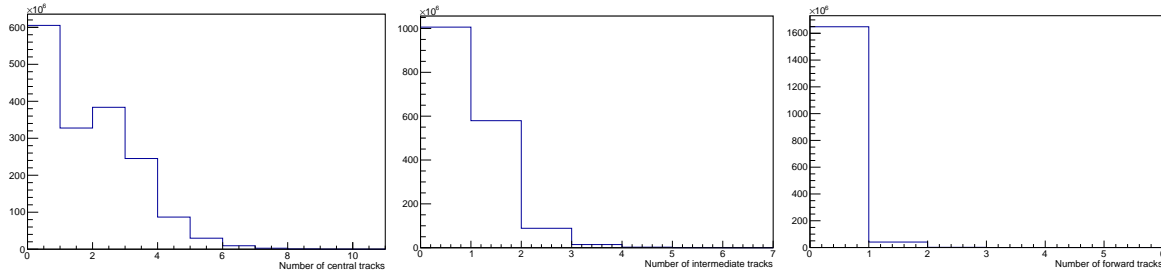


Figure 5.1: Number of tracks in the central-, intermediate- and forward region of the detector system before selection criteria are applied.

The next step is to separate the proton from other charged particles like charged pions and kaons. As figure 5.2 shows, this can be achieved by selecting particles in the reconstructed mass range from 800 to 1 200 MeV. A small correction is applied to the remaining tracks, compensating for the energy loss from particles travelling through the detector matter, according to energy loss the Bethe-Bloch formula.

### 5.2 Identification of the $\pi^0$ and $\eta$ meson

The identification of the mesons is a bit more complex compared to the proton. As shown in table 5.1 the mesons have either major hadronic decay modes or decay dominantly via electromagnetic interaction, resulting in very short lifetimes. The lifetimes of both mesons are in fact short enough for a decay before reaching the detector wall and they consequently have to be recreated from

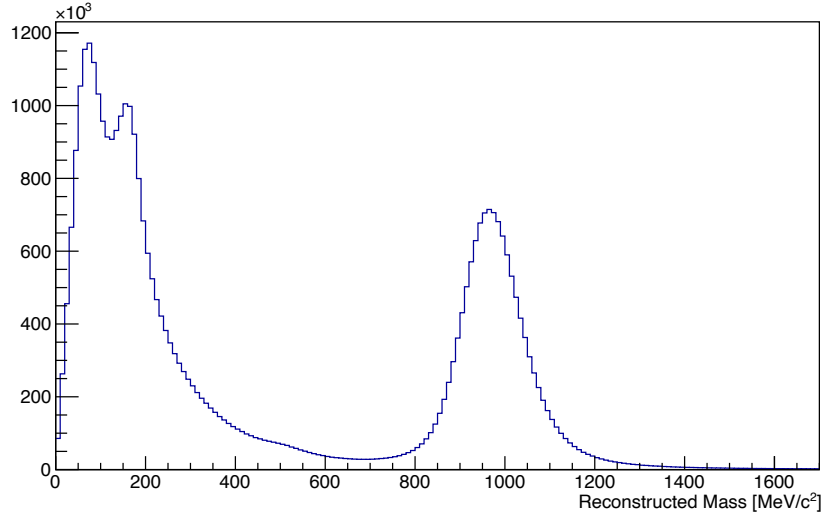


Figure 5.2: Reconstructed mass distribution of particles measured in the forward spectrometer. Protons and pions are identified clearly at their respective masses, as well as a very small kaon contribution. The structure left to the pion peak is caused by positrons, created via pair production from the photon beam in the open drift space.

their decay products. Therefore, the event selection has to be oriented towards the final state particles of the decay modes. For  $\pi^0$ , with its nearly exclusive decay into  $2\gamma$ , the situation is very clear, whereas for the  $\eta$  there are a few more options to choose for reconstruction. With respect to the kinematics of the reaction and the presence of the BGO calorimeter in the central detector part, being optimized for photon detection, the charged modes as well as the  $3\pi^0$  are rejected. Latter one due to the difficulty of catching and separating all six additional photons from the pions. That leaves the  $2\gamma$  modes as the favourable one.

| Particle | Mode          |                    | Fraction ( $\Gamma_i/\Gamma$ ) |
|----------|---------------|--------------------|--------------------------------|
| $\pi^0$  | $\Gamma_1$    | $2\gamma$          | $(98.823 \pm 0.034)\%$         |
|          | $\Gamma_2$    | $e^+e^-\gamma$     | $(1.174 \pm 0.035)\%$          |
| $\eta$   | neutral modes |                    | $(72.12 \pm 0.34)\%$           |
|          | $\Gamma_1$    | $2\gamma$          | $(39.41 \pm 0.20)\%$           |
|          | $\Gamma_2$    | $3\pi^0$           | $(32.68 \pm 0.23)\%$           |
|          | charged modes |                    | $(27.89 \pm 0.29)\%$           |
|          | $\Gamma_3$    | $\pi^+\pi^-\pi^0$  | $(22.92 \pm 0.28)\%$           |
|          | $\Gamma_4$    | $\pi^+\pi^-\gamma$ | $(4.22 \pm 0.08)\%$            |

Table 5.1: Decay modes with the highest branching ratios of the  $\pi^0$  and  $\eta$  meson[8]

In summary we expect four photons in the central spectrometer, two from each meson decay. Events are filtered by requiring four central tracks with energy deposition in the BGO calorimeter, but without a detection in the scintillator barrel, to exclude other charged particles. The distribution of the number



of central tracks can be seen in figure 5.1. Hereafter the central tracks of the remaining events can be interpreted as photons and now have to be assigned to their respective mesons. For this purpose they are grouped into two pairs, whose photons are recombined into particles  $P_1$  and  $P_2$ . Combinatorics provides six configurations of possible pairs, the invariant mass distributions for all combinations of the particles are shown in figure 5.3. Yet only three of the combinations are independent leading to the diagonal symmetry in the histogram.

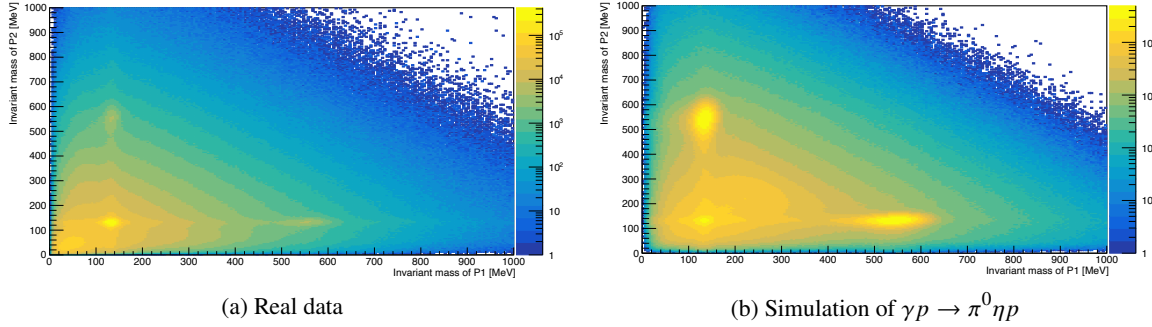


Figure 5.3: Two-dimensional histogram of the invariant masses of recombined particles  $P_1$  and  $P_2$ .

In the histogram created from the real data set the two narrow, two-dimensional peaks corresponding to  $\pi^0$  and  $\eta$  are clearly visible. A next logical step could be to only maintain events, where the particle masses of  $P_1$  and  $P_2$  are close to the masses of the expected  $\pi^0$  and  $\eta$  mesons, equivalent to graphically perform a box shaped selection around one of the two peaks. The figure 5.4 shows the invariant mass distributions of the particles  $P_1$  and  $P_2$  with a selection on the invariant mass of the respective other particle.

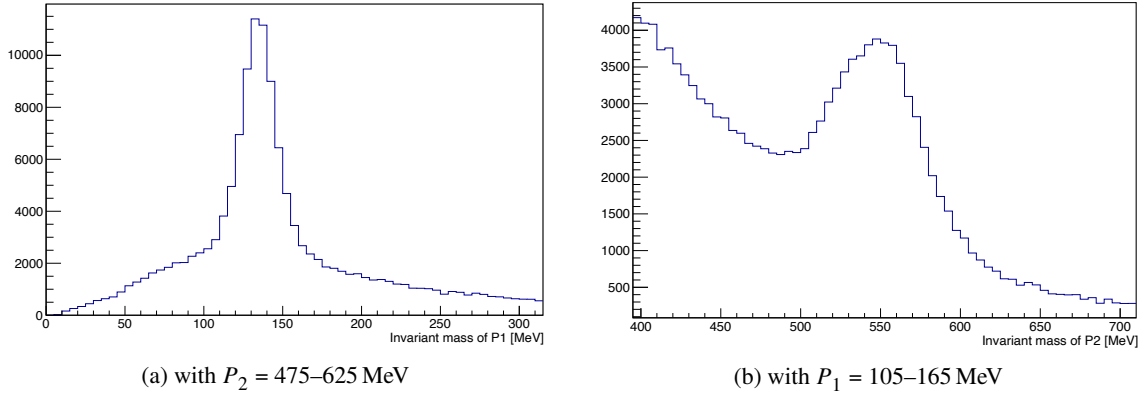


Figure 5.4: Invariant mass distributions of  $P_1$  and  $P_2$  with a selection on the respective other invariant particle mass. The particle  $P_1$  here corresponds to the  $\pi^0$  and the particle  $P_2$  to the  $\eta$ .

However, these histograms, as well as the conspicuous peak, located at the bottom left of the real data histogram, implies that there is background mainly from channels including multiple  $\pi^0$  particles. Despite their technically lower invariant mass of  $P_1$  and  $P_2$ , these background channels expand to some extent in the mass region of the  $\eta$  and can not be neglected by just setting the invariant mass as a

selection criteria, due to their high cross sections. Possible background includes:

$$\text{Background Channel 1: } \gamma p \rightarrow \pi^0 \pi^0 p$$

$$\text{Background Channel 2: } \gamma p \rightarrow \pi^0 \pi^0 \pi^0 p$$

The distributions of the invariant masses of the recreated particles for these channels are shown in figure 5.5.

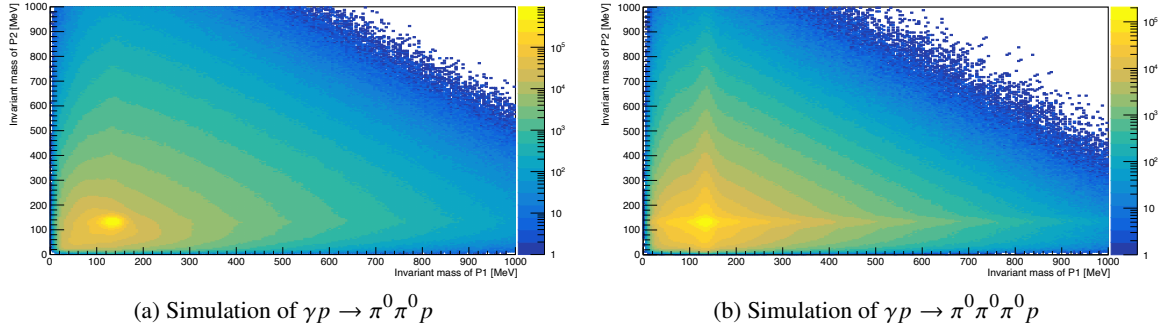


Figure 5.5: Two-dimensional histogram of the invariant masses of recombined particles  $P_1$  and  $P_2$  for both background channels. The phenomenon of two or more photons being measured as one for the channel  $\gamma p \rightarrow \pi^0 \pi^0 \pi^0 p$  manifests itself as vertical and horizontal lines.

Regarding the background channel  $\gamma p \rightarrow \pi^0 \pi^0 \pi^0 p$  there are a few more things to consider. It should be noted that this channel is promoted by the sequential decay of an  $\eta$  particle from the reaction channel  $\gamma p \rightarrow \eta p \rightarrow \pi^0 \pi^0 \pi^0 p$ . Furthermore, the event selection requires four photons, thus two of the six photons from the  $\pi^0$  decays either have to be missed by the detector or need to be too close to distinguish them from other photons. The probability of this happening is about 25%. The latter effect then causes events where the deposited energy of two or more photons is readout as one higher energetic photon, the recombined particles  $P_1$  and  $P_2$  consequently tend to have a higher invariant masses, making a separation from  $\gamma p \rightarrow \pi^0 \eta p$  even harder. For these reasons, the following steps of the event selection mainly focusses on filtering out the channel  $\gamma p \rightarrow \pi^0 \pi^0 p$ , whereas the  $\gamma p \rightarrow \pi^0 \pi^0 \pi^0 p$  channel is separated in a later step of the analysis (6.1).

During the course of this thesis various techniques had been tried out, the most promising one turned out to be V. L. Kashevarov's from a paper in 2009 [33]. Here the deviations  $\chi_{2\pi}$  and  $\chi_{\pi\eta}$  from the particle masses  $m_{\pi^0}$  and  $m_\eta$  of their respective two-meson final states are calculated and weighted, based on the corresponding invariant-mass resolutions  $\sigma_{\pi^0}$  and  $\sigma_\eta$  of the detector system:

$$\chi_{2\pi} = \sqrt{\left(\frac{M_{\gamma_i \gamma_j} - m_{\pi^0}}{\sigma_{\pi^0}}\right)^2 + \left(\frac{M_{\gamma_k \gamma_l} - m_{\pi^0}}{\sigma_{\pi^0}}\right)^2} \quad (5.1)$$

$$\chi_{\pi\eta} = \sqrt{\left(\frac{M_{\gamma_i \gamma_j} - m_{\pi^0}}{\sigma_{\pi^0}}\right)^2 + \left(\frac{M_{\gamma_k \gamma_l} - m_\eta}{\sigma_\eta}\right)^2} \quad (5.2)$$

This is done for every independent combination of recombined  $P_1$  and  $P_2$ , the sigma values at

the BGOOD experiment for  $\pi^0$  and  $\eta$  are approximately 12 MeV and 25 MeV respectively[6]. The distributions of  $\chi_{\pi\eta}$  values for the real data and the different simulated reaction channels are presented in figure 5.6.

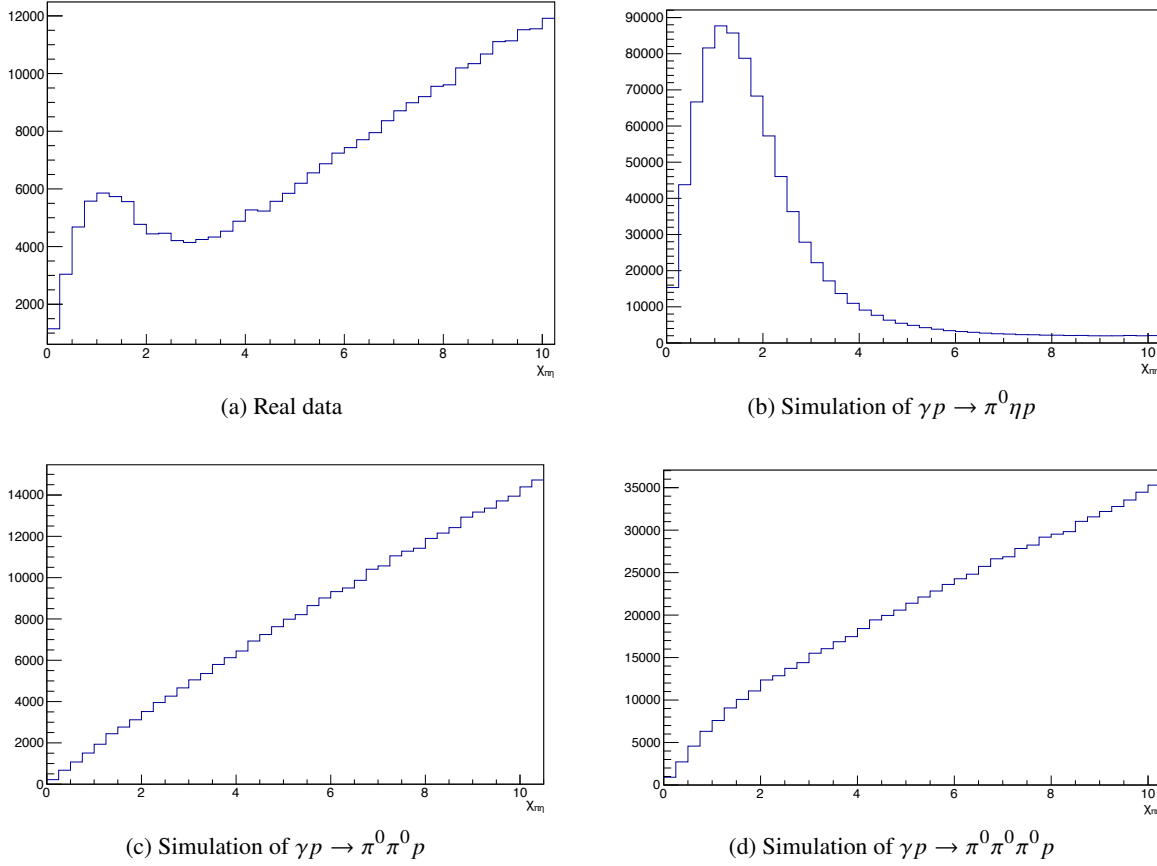
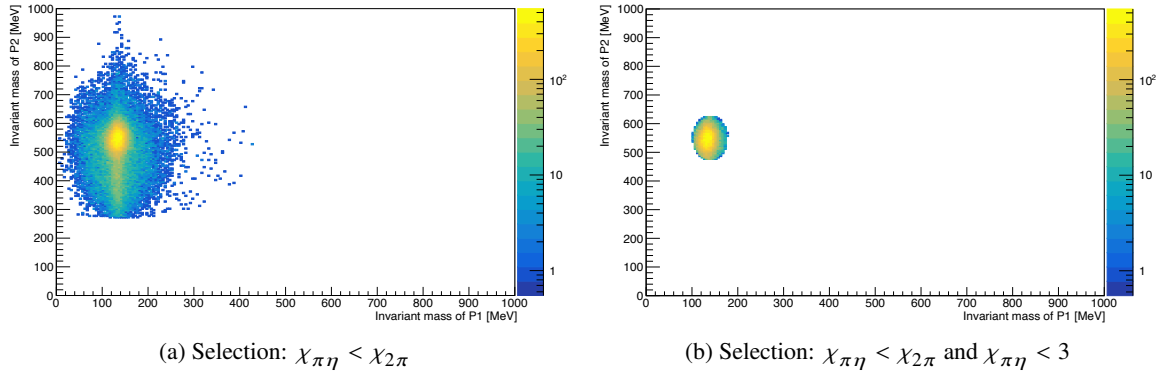
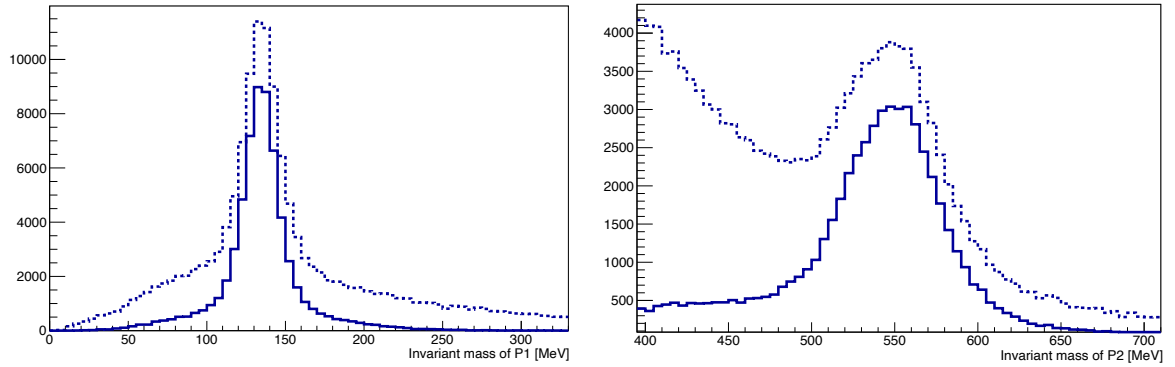


Figure 5.6: Distributions of  $\chi_{\pi\eta}$  values.

The smallest  $\chi_{\pi\eta}$  and  $\chi_{2\pi}$  value is stored and each event is subsequently assigned either to the  $\pi^0 \pi^0$  or the  $\pi^0 \eta$  channel, depending on the minimum  $\chi$  value. Events with smaller deviation to  $\pi^0 \pi^0$  are rejected, the remaining ones, shown in figure 5.7(a) form a clear two-dimensional peak corresponding to  $\pi^0$  and  $\eta$ . Results of the invariant mass distribution of the both mesons compared to a selection based on figure 5.3(a), without rejecting the background, are shown in figure 5.8. Aside from the distribution of the particle  $P_2$  corresponding to the  $\eta$ , still showing a small amount of background, the rejection works quite well. Finally an additional selection of events with  $\chi_{\pi\eta} < 3$  is done. This manifests itself as an ovally shaped cutout in the two-dimensional histogram 5.7(b) and ensures the focus of events with low deviation from the signal channel.

### 5.3 Combined Selection

Since the participants of the reaction were identified in different detector parts, a next logical step to combine the information is to compare the reaction kinematics and ensure the absence of other


 Figure 5.7: Two-dimensional histogram of the invariant masses of recombined particles  $P_1$  and  $P_2$ 

 Figure 5.8: Invariant masses of the recombined particles  $P_1$ , corresponding to the  $\pi^0$ , and  $P_2$ , corresponding to the  $\eta$  before the background rejection (dotted line) and afterwards (solid line).

unwanted particles. This is done in two steps. With the well known photon energy from the tagger and the assumption, that the proton possesses no momentum at the start of the reaction, it is possible to calculate an initial state four vector. Afterwards a check for coincidence between the detector parts can be made by either subtracting the four-vectors of both mesons from the initial state, leaving the missing part in the central detector, that should correspond to the proton measured in the forward spectrometer, or subtracting the four vector of the proton, leaving the missing part in the forward spectrometer, that should correspond to both mesons measured in the central detector:

$$P_{\text{missing}} = P_{\text{initial state}} - P_{\text{measured}} \quad (5.3)$$

The simpler, first option is preferred here. Figure 5.9 shows the distribution of difference in  $\theta$  angle between the missing part in the central detector and the forward proton, which is centred around zero, as well as the opening angle  $\delta$  between both vectors. Events with opening angles greater than  $10^\circ$  are removed. Regarding the mass and momentum, there is a clear accumulation of events with low difference at lower beam energies shown in figure 5.10, yet it is hard to exclude the ones with high differences here, due to the natural spreading of the distribution at higher energies.

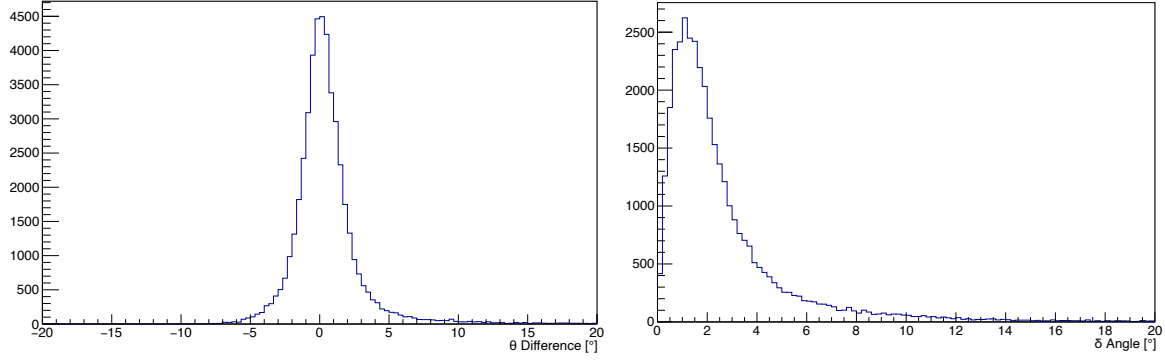


Figure 5.9: Difference in  $\theta$  angle (left) between missing mass of the central detector and the forward proton and opening angle  $\delta$  (right) between both vectors.

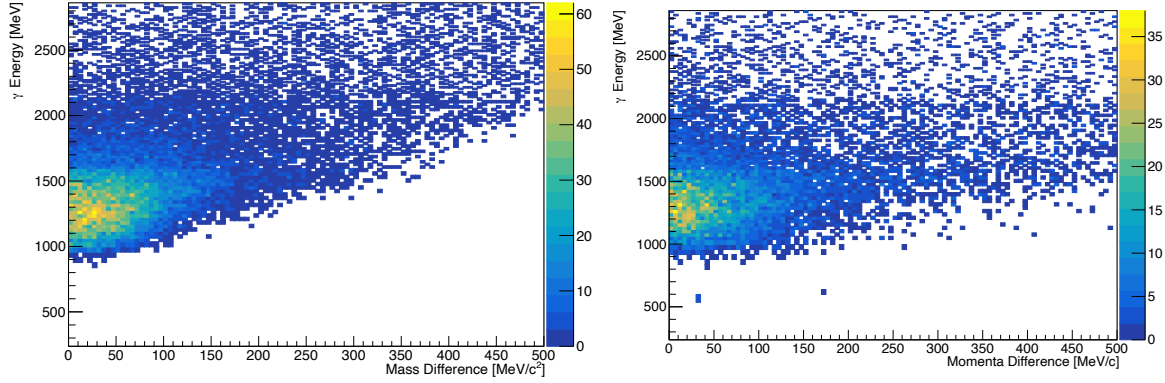


Figure 5.10: Distribution of the difference in mass (left) and momentum (right) between the forward proton and the central missing mass against beam energy.

| Selection criterium           | Value                             | Acceptance (%) | Total Events<br><b><math>1.691 \times 10^9</math></b> |
|-------------------------------|-----------------------------------|----------------|---|
| Number of forward tracks      | 1 (+ charged)                     | 2.418          | $40.90 \times 10^6$                                   |
| Reconstructed forward mass    | 800–1 200 MeV                     | 30.93          | $12.65 \times 10^6$                                   |
| Number of intermediate tracks | 0                                 | 80.65          | $10.20 \times 10^6$                                   |
| Number of central tracks      | 0 ( $\pm$ charged), 4 (uncharged) | 5.274          | $538.2 \times 10^3$                                   |
| Deviation $\chi_{\pi\eta}$    | $\chi_{\pi\eta} < \chi_{\pi\pi}$  | 11.54          | $62.13 \times 10^3$                                   |
| Deviation $\chi_{\pi\eta}$    | $\chi_{\pi\eta} < 3$              | 65.87          | $40.93 \times 10^3$                                   |
| $\delta$ Angle                | $\delta < 10$                     | 95.98          | $39.28 \times 10^3$                                   |
| $2.323 \times 10^{-3}$        |                                   |                | <b><math>39.28 \times 10^3</math></b>                 |

Table 5.2: Acceptance of the selection criteria and total number of events



## Data analysis

**RooFit** Data analysis in this thesis is done using RooFit. The RooFit library is a toolkit implemented in the ROOT data analysis framework for modeling of event data distributions. A given distribution can be described by a composition of multiple probability density functions (PDFs). These can be built up from the Monte Carlo simulations, are easily added up with fraction coefficients and allow for separation of the single components of a distribution. In the following sections, this technique is applied to isolate the signal  $\gamma p \rightarrow \pi^0 \eta p$  from the background  $\gamma p \rightarrow \pi^0 \pi^0 \pi^0 p$  and disentangle the constituents in the invariant mass spectrum of the  $\pi^0 \eta$  system.

### 6.1 Background Separation

So far, the main focus of the event selection was filtering out the background channel  $\gamma p \rightarrow \pi^0 \pi^0 p$ . This obviously removes a lot of the background from  $\gamma p \rightarrow \pi^0 \pi^0 \pi^0 p$  as a benefit, yet a significant amount can not be rejected solely on the invariant mass information of the reconstructed particles  $P_1$  and  $P_2$ , due to the phenomenon explained in section 5.2. Remedy for the problem is the missing mass distribution of the central detector, shown in figure 6.1. There is a clear difference between our signal channel and the background channel allowing a separation.

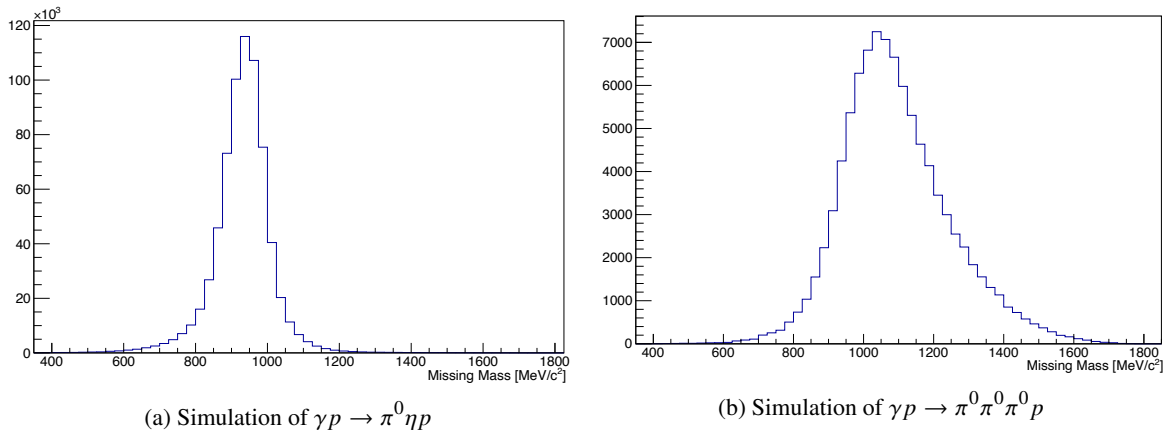


Figure 6.1: Missing mass distributions in the central detector.

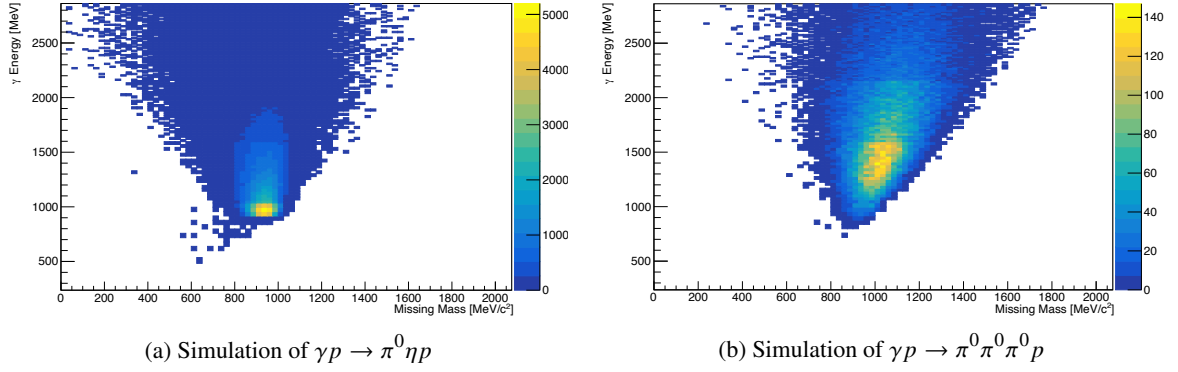


Figure 6.2: Missing mass distributions in the central detector against photon energy  $E_\gamma$ . The ratio of the signal channel to the background channel decreases with higher photon energies.

The PDFs of both channels are formed by simulated data and adjusted in height to the real data distribution by fraction coefficients. This procedure is done binwise for every beam energy bin. By looking at the figure 6.2 one expects an increase in ratio of the background channel to the signal channel with higher energies, as well as a shift to larger missing masses for the background channel. The fits for different photon energies, shown in figure 6.3, match really well with the real data set and confirm this expectation.

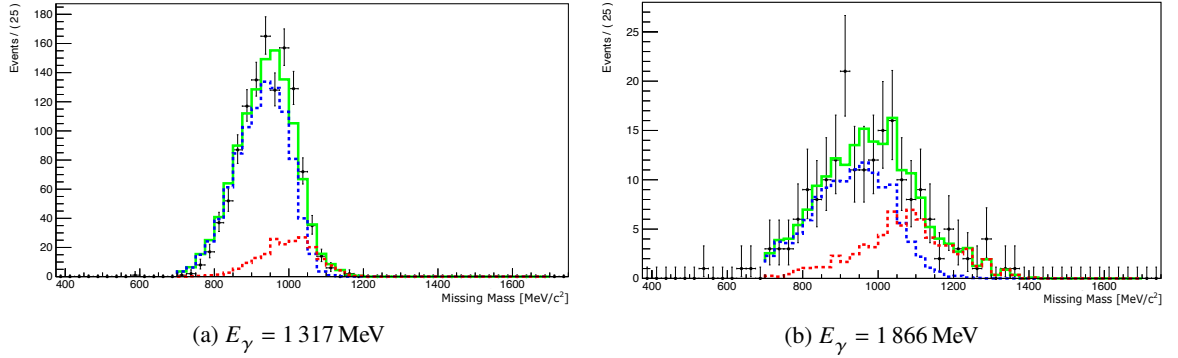


Figure 6.3: The signal channel, background channel and sum total are shown as the blue, red and green line respectively.

## 6.2 Determination of the differential cross section

In context of classical scattering experiments the cross section can be depicted as the overlap area for the two colliding objects. It is proportional to the probability of a specific process to take place. Because of the BGOOD experiment is a fixed target experiment that provides excellent resolution and high statistics at forward angles of the proton, it is reasonable to specify the cross section in the differential limits of the proton angle. The differential cross section is defined by the number of particles  $N_{sc}$  scattered into an element of solid angle  $d\Omega$  in the directions  $\theta$  and  $\phi$  per unit time, the



target area density  $\rho_{\text{target}}$  and the incoming particle flux  $I_{\text{inc}}$ :

$$\frac{d\sigma}{d\Omega}(\theta, \phi) = \frac{dN_{\text{sc}}}{d\Omega I_{\text{inc}} \rho_{\text{target}}} \quad (6.1)$$

In case of a cylindrically symmetric system, the cross sections is equally distributed in azimuthal angle  $\phi$ , therefore, it makes sense to integrate over the full angular range in  $\phi$ . The solid angle can be written as:

$$d\Omega = \int_0^{2\pi} d\phi \int_{\theta_1}^{\theta_2} \sin(\theta) d\theta = 2\pi [\cos(\theta_1) - \cos(\theta_2)] \quad (6.2)$$

Assuming the differential cross section is approximately constant over a small solid angle range and with respect to the distribution, shown in figure 6.4(a), a differential limit is set for events with  $\cos(\theta_{\text{cms}}^P)$  of 0.8 or greater. This includes the major portion of the events, the expression of the solid angle then becomes  $d\Omega = 0.4\pi$ . It should be noted that differential cross sections calculations are generally easier to perform within the center-of-mass frame (cms) and differ from calculations in laboratory frame, since the scattering angle  $\theta$  is frame dependent. Considering the dependence on the single photon energy  $E_\gamma$  of some of the parameters the differential cross section at the BGOOD experiment is more specifically described by:

$$\frac{d\sigma}{d\Omega}(E_\gamma, \theta) = \frac{dN_{\text{sc}}(E_\gamma, \theta)}{d\Omega I_{\text{inc}}(E_\gamma) \rho_{\text{target}}} \cdot \frac{1}{\epsilon_{\text{det}}(E_\gamma, \theta)} \quad (6.3)$$

The additional expression equalizes for the detector efficiency  $\epsilon_{\text{det}}$  being lower the 100% due to the limited detector acceptance and selection criteria. The determination of the detector efficiency, the target area density and the incident particle flux are explained in the following paragraphs.

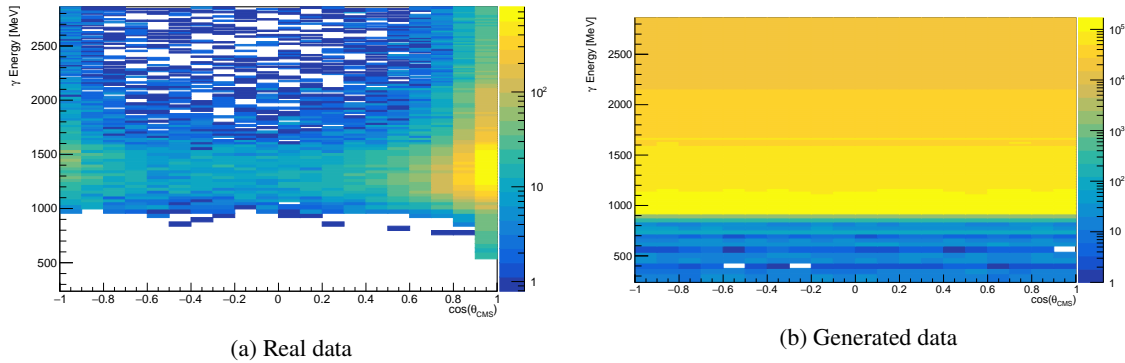


Figure 6.4: Distribution in solid angle against beam energy. The generated data is distributed equally over all solid angles. This changes when information of the ExPIORA data base, like detector geometry and magnetic, fields is applied in simulation.

**Detector efficiency** The detector efficiency  $\epsilon_{\text{det}}$  describes the probability of a reaction to be measured by the detector system. It is defined by the ratio of identified reactions to the total number of reactions occurring, and consequently varies for different energies and reaction channels depending on their kinematical agreement with the detector coverage. In case of a real data set the exact number of total

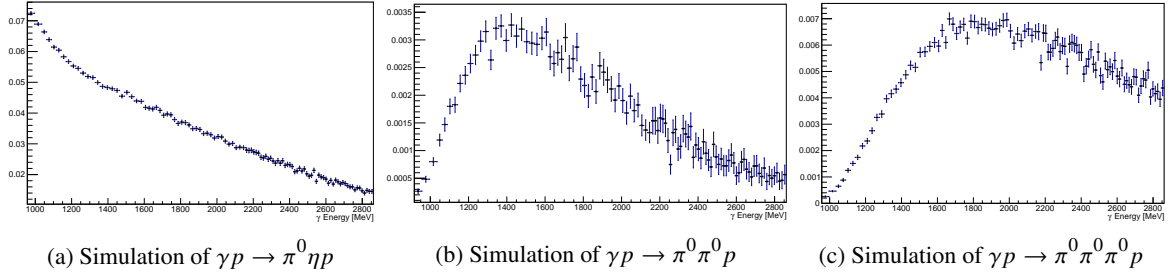


Figure 6.5: Detector efficiency and false detection probabilities for the identification of the reaction channel  $\gamma p \rightarrow \pi^0 \eta p$

reactions is unknown (or can only be estimated by predictions), a logical solution to the problem is to generate simulated data. Here the total number of reactions is known by the number of generated reactions  $N_{\text{gen}}$ . The number of identified reactions  $N_{\text{sim}}$  for a generated data set is determined by simulation like described in section 4.1 and thus affected by the detector characteristics and geometry, as well as the event selection methods. The efficiency can then be defined by:

$$\epsilon_{\text{det}} = \frac{N_{\text{sim}}}{N_{\text{gen}}} \quad (6.4)$$

Figure 6.5 shows the detector efficiency  $\epsilon_{\text{det}}$  for the desired reaction channel  $\gamma p \rightarrow \pi^0 \eta p$ , as well as the probabilities for the background channels  $\gamma p \rightarrow \pi^0 \pi^0 p$  and  $\gamma p \rightarrow \pi^0 \pi^0 \pi^0 p$  to be detected as the signal channel. The identification for all three efficiencies is done by the selection criteria from section 5, before the fit to the missing mass distribution is performed. The efficiency for  $\gamma p \rightarrow \pi^0 \eta p$  decreases from 7% to under 2% at high energies. The false detection probabilities of the background channels are, as expected, smaller by a magnitude.

**Photon Flux** The photon flux is measured by tagger-system and the detectors GIM and FluMo. The technique of monitoring the photon flux at high intensities is explained in section 3.2.1. The distribution of the photon flux for the 2017 beam time is shown in figure 6.6. The flux appears to be much higher at low energies. This is in fact the case, however, it has to be taken into account, that the energy width of the bins increases at lower beam energies. This phenomenon originates from the tagging-system's restriction in space and is described in section 3.2.1 and results in vertical steps in the distribution.

**Target density** The area density  $\rho_{\text{target}}$  is given by the relation:

$$\rho_{\text{target}} = n \cdot z \quad (6.5)$$

where  $n$  is the target density and  $z$  the target cell length. With the known density for liquid hydrogen at 18 K the target area density is determined to be  $2.58 \times 10^{-7} \mu\text{b}^{-1}$  in the PhD thesis of Georg Scheluchin[23].

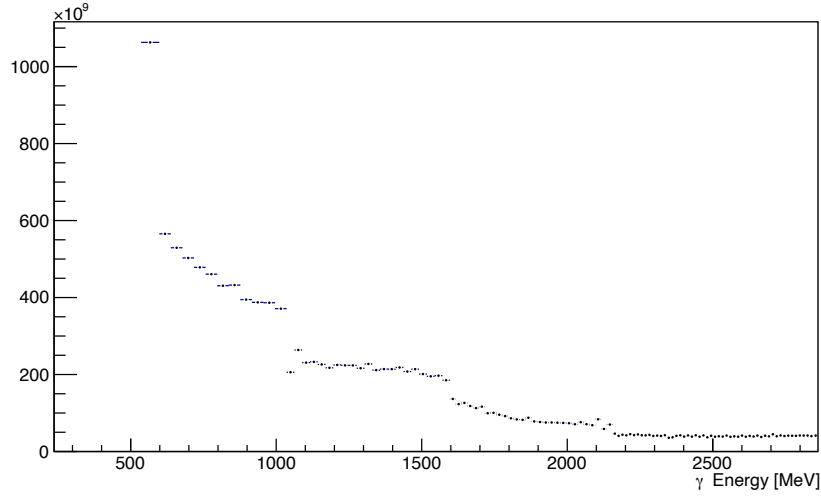


Figure 6.6: Photon flux present at the target.

### 6.2.1 Systematic uncertainties

The various sources responsible for systematic uncertainties in this analysis are listed in table 6.1.

| Source                            | % Error    |
|-----------------------------------|------------|
| Proton identification             | 5.0        |
| Beam spot alignment               | 4.0        |
| Photon flux                       | 4.0        |
| SciFi efficiency                  | 3.0        |
| Target wall contribution          | 2.0        |
| Track time selection              | 2.0        |
| Target length                     | 1.7        |
| ToF wall efficiency               | 1.5        |
| MOMO efficiency                   | 1.0        |
| Drift chamber efficiency          | 1.0        |
| Beam energy calibration           | 1.0        |
| Modeling of hardware triggers     | 1.0        |
| $\pi^0$ identification            | 1.0        |
| Forward track geometric selection | 1.0        |
| $\eta$ identification             | 1.5        |
| Fitting uncertainty               | $\sim 1.0$ |
| Summed in square                  | 9.4        |

Table 6.1: Systematic uncertainties of the differential cross section measurement (based on [6][34]).

Most of the values were determined previously in the references [6] and [34]. The largest contributions originate from identifying the proton (this can be decreased to 1% with further analysis), the position of the beam when impinging upon the target, closely related to the production angle, and the absolute photon flux determination, followed by smaller uncertainties of the other detector components. The

uncertainties of identifying the  $\eta$ , as well as the fitting uncertainty are estimated. Because of the fitting uncertainty not varying much and only making up for a small fraction of the total systematic uncertainty, one can assume that the total systematic uncertainty is a constant fraction of the measured cross section.

### 6.2.2 Differential cross section of the uncorrelated $\gamma p \rightarrow \pi^0 \eta p$ channel

Previous steps of this analysis reject the different background channels. The number of events  $N_{\pi^0 \eta}$  belonging to the  $\gamma p \rightarrow \pi^0 \eta p$  channel can be extracted as the integral of the signal distribution in figure 6.3. This has to be done binwise for every energy. To determine the differential cross section of the channel the general number of scattered particles into an element of solid angle  $N_{sc}$  in equation 6.3 can be replaced by  $N_{\pi^0 \eta}$ . Including the results for detector efficiency, photon flux and target area density the differential cross section is shown in figure 6.7:

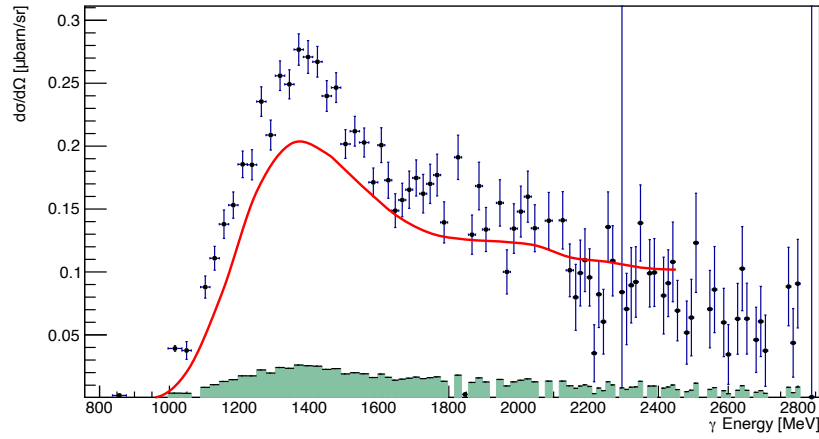


Figure 6.7: Differential cross section of the  $\gamma p \rightarrow \pi^0 \eta p$  channel (blue dots) and the systematic error (filled green) in  $\cos(\theta_{cms}^p) > 0.8$ . The data is compared to the BnGa-PWA (red line)[35]

A good reference for comparison is the differential cross section determined by the Bonn-Gatchina partial wave analysis (BnGa-PWA)[35] in the two solid angle bins  $\cos(\theta_{cms}^p) > 0.8$ . The data set used in the histogram is the smoothed average from both solid angle bins extracted for 16 different energies in the range 950 to 2450 MeV. The cross sections shows good agreement in form and height, except deviations of up to 25% in the region around 1400 MeV. The deviation could result from remaining event migration of the  $\gamma p \rightarrow \pi^0 \pi^0 p$  channel, whose false detection probability peaks exactly at this energy. A significantly more precise rejection of this channel can be achieved by including the detector resolution of the angle and momentum, this allows a likelihood fitting to the optimal values referred to as a *kinematic fit*. This could not be performed in the time frame of the thesis.

### 6.2.3 Differential cross section of the $\gamma p \rightarrow a_0(980) p \rightarrow \pi^0 \eta p$ channel

As explained in the introduction, a correlation between the  $a_0(980)$ , the  $a_2(1320)$  and the  $\gamma p \rightarrow \pi^0 \eta p$  channel is expected, since both resonances have dominant neutral decay modes, that should contribute

to the  $\pi^0\eta$  invariant mass spectrum at a certain energy range:

$$\begin{aligned}\gamma p &\rightarrow a_0(980)p \rightarrow \pi^0\eta p \\ \gamma p &\rightarrow a_2(1320)p \rightarrow \pi^0\eta p\end{aligned}$$

This correlation should show up as a peak in the spectrum, located at the respective mass of the resonance. To disentangle the contributions of the uncorrelated  $\pi^0\eta$  channel, the  $a_0(980)$  and  $a_2(1320)$  the decays of both resonances are simulated, the invariant mass distributions against beam energy are presented in figure 6.8.

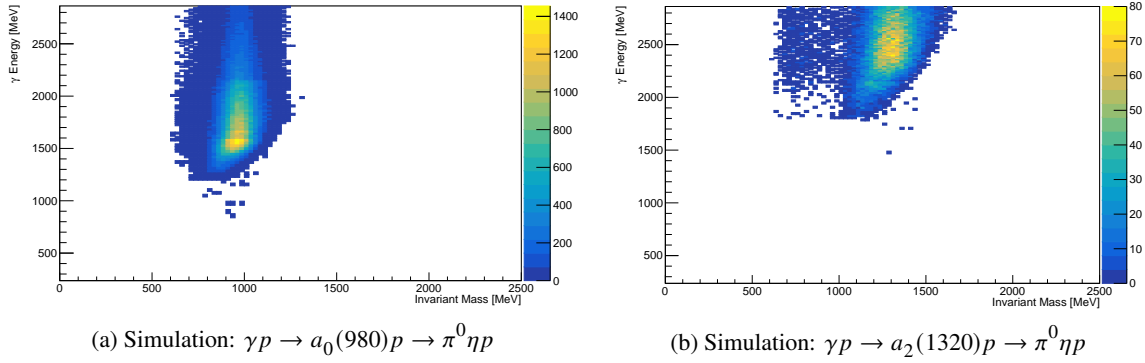


Figure 6.8: Invariant mass distributions against beam energy of the sequential decay of  $a_0(980)$  and  $a_2(1320)$ .

The production thresholds are located at the expected photon energies from section 2.3. An isolation from the uncorrelated channel is done by RooFit. In the following four bins are combined into one, because of statistics being too low to perform a good fit for every energy bin. Two examples for different energies are shown in figure 6.9.

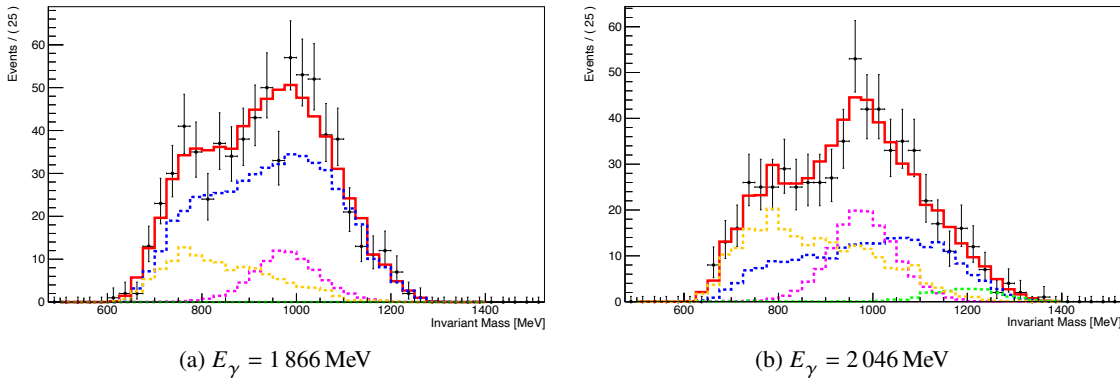


Figure 6.9: Invariant mass distribution of the  $\pi^0\eta$  system from real data (black) compared to the sum (red) of the different contributions from the  $\gamma p \rightarrow \pi^0\pi^0 p$  background (orange), the uncorrelated  $\gamma p \rightarrow \pi^0\eta p$  channel (blue), the  $a_0(980)$  (magenta) and the  $a_2(1320)$  (green).

The  $a_0(980)$  contribution is clearly identified here, the peak is located exactly at the expected invariant mass. The  $a_2(1320)$  contribution is harder to isolate, due to statistics strongly decreasing at beam energies above 2 GeV. Nevertheless, a small amount is sighted in some of the fits, like 6.9(b).

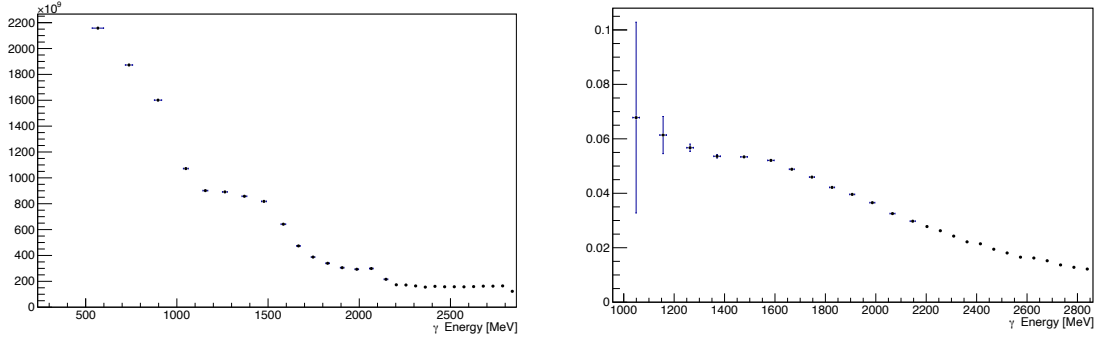


Figure 6.10: The detection efficiency (left) and photon flux (right) of the  $\gamma p \rightarrow a_0(980)p \rightarrow \pi^0 \eta p$  channel.

With the known contribution of the  $a_0(980)$  it is possible to determine the differential cross section of the  $\gamma p \rightarrow a_0(980)p \rightarrow \pi^0 \eta p$  channel. For this purpose it is necessary to extend the rebinning of four energy bin into one to the photon flux and determine a detection efficiency for the channel. The re-binned flux and the detection efficiency are shown in figure 6.10, the preliminary cross section is shown in figure 6.11.

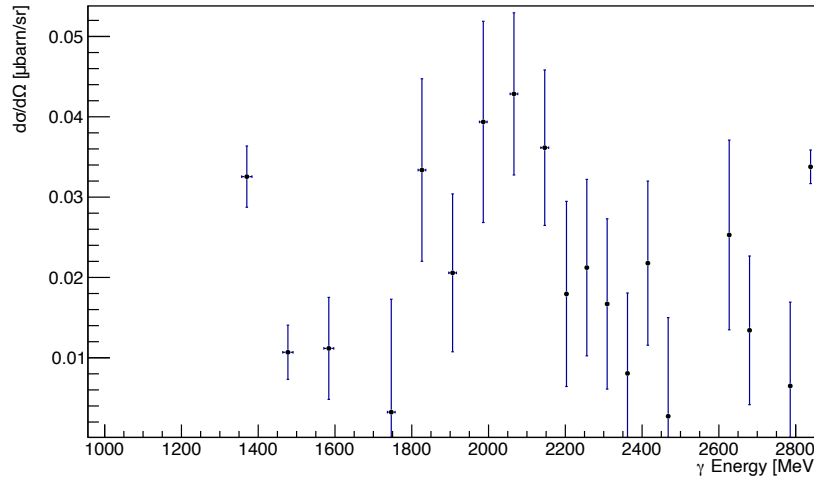


Figure 6.11: Differential cross section of the  $\gamma p \rightarrow a_0(980)p \rightarrow \pi^0 \eta p$  channel in  $\cos(\theta_{\text{cms}}^p) > 0.8$ .

Some of the bins of the differential cross section are clearly outside of a sensible range, due to inaccuracies in the fits. RooFit is very sensitive to errors which can happen, when the difference between the PDFs is not clear enough to perform a successful fit, or the statistics are too low. In some cases the fits can be corrected manually by adjusting the fit parameters or fit ranges, in other cases the fits could not be fixed that easily. This differential cross section, therefore, can be considered as very preliminary, but as a proof of principle that the  $a_0(980)$  photoproduction cross section can be determined by the BGOOD experiment.

## Summary and outlook

The goal of this thesis was to study the reaction mechanisms of the  $a_0(980)$  and the  $a_2(1320)$  in photoproduction, to determine their cross sections and disentangle them from other broad and overlapping resonances in the light quark sector. For this purpose the reaction channel  $\gamma p \rightarrow \pi^0 \eta p$  was studied in depth. The event selection of the final state mesons and the proton works really well, the background channel  $\gamma p \rightarrow \pi^0 \pi^0 p$  is removed for the most part. Here a more precise rejection could be achieved by a kinematic fit. Due to the short time frame of the thesis this was not realizable. The background channel  $\gamma p \rightarrow \pi^0 \pi^0 \pi^0 p$  is separated in the missing mass distribution by using the RooFit toolkit. The differential cross section of the uncorrelated  $\gamma p \rightarrow \pi^0 \eta p$  channel was determined and shows good agreement with the Bonn-Gatchina partial wave analysis, aside from the energy region around 1 400 MeV.

The contribution of the  $a_0(980)$  in the invariant mass distribution of the  $\pi^0 \eta$  system was determined and a contribution of the  $a_2(1320)$  was sighted in some of the fits. The cross section determination of the sequential  $\gamma p \rightarrow a_0(980) p \rightarrow \pi^0 \eta p$  channel is performed successfully for the bins where the fit to the invariant mass distribution works. A cross section calculation of the  $\gamma p \rightarrow a_2(1320) p \rightarrow \pi^0 \eta p$  was not possible as a consequence of too low statistics at the higher beam energies above 2 GeV.

These results provide a first exploratory study into the photoproduction of a  $\pi^0 \eta$  pair on a proton at the BGOOD experiment. They show that the experiment is capable of high quality measurements of the  $a_0(980)$  resonance and likely, if more data is acquired in the high energy ranges, of the  $a_2(1320)$  resonance.





## Bibliography

---

- [1] S. K. Choi et al.,  
*Observation of a narrow charmonium-like state in exclusive  $B^\pm \rightarrow K^\pm \pi^+ \pi^- J/\psi$  decays*,  
*Phys. Rev. Lett.* **91** (2003) 262001, arXiv: [hep-ex/0309032](#) (cit. on p. 2).
- [2] J. Ajaka et al., *Simultaneous Photoproduction of  $\eta$  and  $\pi^0$  Mesons on the Proton*,  
*Phys. Rev. Lett.* **100** (5 2008) 052003,  
URL: <https://link.aps.org/doi/10.1103/PhysRevLett.100.052003> (cit. on p. 2).
- [3] Kashevarov, V.L. et al.,  
*First measurement of the circular beam asymmetry in the  $\gamma p \rightarrow \pi^0 \eta p$  reaction*,  
*Physics Letters B* **693** (2010) 551, ISSN: 0370-2693,  
URL: <http://dx.doi.org/10.1016/j.physletb.2010.09.028> (cit. on p. 2).
- [4] Horn, I. et al., *Study of the reaction  $\gamma p \rightarrow \pi^0 \eta p$* , *Eur. Phys. J. A* **38** (2008) 173,  
URL: <https://doi.org/10.1140/epja/i2008-10657-7> (cit. on p. 2).
- [5] A. Celentano et al.,  
*First measurement of direct photoproduction of the  $a_2(1320)$  meson on the proton*,  
*Phys. Rev. C* **102** (2020) 032201, arXiv: [2004.05359 \[nucl-ex\]](#) (cit. on p. 2).
- [6] S. Alef et al., *The BGOOD experimental setup at ELSA*, *Eur. Phys. J. A* **56** (2020) 104,  
arXiv: [1910.11939 \[physics.ins-det\]](#) (cit. on pp. 2, 15–18, 21, 31, 37, 45).
- [7] *Standard Model*, Wikipedia (2021),  
URL: [https://en.wikipedia.org/wiki/Standard\\_Model](https://en.wikipedia.org/wiki/Standard_Model) (visited on 09/09/2021)  
(cit. on p. 3).
- [8] P. A. Zyla et al., *Review of Particle Physics*,  
*Progress of Theoretical and Experimental Physics* **2020** (2020), 083C01, ISSN: 2050-3911,  
eprint: <https://academic.oup.com/ptep/article-pdf/2020/8/083C01/34673722/ptaa104.pdf>,  
URL: <https://doi.org/10.1093/ptep/ptaa104> (cit. on pp. 6, 9–11, 14, 34).
- [9] B. Povh et al., *Teilchen und Kerne*, vol. 9, Springer Spektrum, 2014 (cit. on p. 7).
- [10] *Baryon*, Wikipedia (2021),  
URL: <https://de.wikipedia.org/wiki/Baryon> (visited on 08/09/2021) (cit. on p. 9).
- [11] *Meson*, Wikipedia (2021),  
URL: <https://de.wikipedia.org/wiki/Datei:Meson-octet-small.svg> (visited on 08/09/2021) (cit. on p. 10).
- [12] Z.-G. Wang, *Analysis of the scalar nonet mesons with QCD sum rules*,  
*The European Physical Journal C* **76** (2016), ISSN: 1434-6052,  
URL: <http://dx.doi.org/10.1140/epjc/s10052-016-4262-y> (cit. on p. 11).

- [13] R. J. Jaffe, *Multiquark hadrons. I. Phenomenology of  $Q^2\overline{Q}^2$  mesons*, *Phys. Rev. D* **15** (1 1977) 267,  
URL: <https://link.aps.org/doi/10.1103/PhysRevD.15.267> (cit. on pp. 11, 13).
- [14] J. Weinstein and N. Isgur, *Do Multiquark Hadrons Exist?*, *Phys. Rev. Lett.* **48** (10 1982) 659,  
URL: <https://link.aps.org/doi/10.1103/PhysRevLett.48.659> (cit. on p. 11).
- [15] G. Janssen et al., *Structure of the scalar mesons  $f_0(980)$  and  $a_0(980)$* , *Phys. Rev. D* **52** (5 1995) 2690,  
URL: <https://link.aps.org/doi/10.1103/PhysRevD.52.2690> (cit. on p. 11).
- [16] J. Oller, E. Oset and A. Ramos, *Chiral unitary approach to meson-meson and meson-baryon interactions and nuclear applications*, *Progress in Particle and Nuclear Physics* **45** (2000) 157,  
ISSN: 0146-6410,  
URL: <https://www.sciencedirect.com/science/article/pii/S0146641000001046> (cit. on p. 11).
- [17] N. Wolchover, *Quark Quartet Fuels Quantum Feud*, Quanta Magazine (2014),  
URL: <https://web.archive.org/web/20141014174610/http://www.simonsfoundation.org/quanta/20140827-quark-quartet-fuels-quantum-feud/> (cit. on p. 12).
- [18] M. Karliner, J. L. Rosner and T. Skwarnicki, *Multiquark States*, (2017) (cit. on p. 12).
- [19] C. Amsler et al., *Scalar Mesons below 2 GeV*, Review of Particle Physics (2020),  
URL: <https://pdg.lbl.gov/2021/reviews/rpp2020-rev-scalar-mesons.pdf> (visited on 10/09/2021) (cit. on p. 13).
- [20] F. Frommberger, *Technical overview of ELSA*, 2002,  
URL: <https://www-elsa.physik.uni-bonn.de/Beschleuniger/elsatech.html> (visited on 23/03/2021) (cit. on pp. 16, 17).
- [21] W. Hillert et al., *Beam and spin dynamics in the fast ramping storage ring ELSA: Concepts and measures to increase beam energy, current and polarization*, *EPJ Web Conf.* **134** (2017) 05002, ed. by F. Klein, U. -G. Meißner and U. Thoma (cit. on pp. 16, 17).
- [22] A. Bella, *Linearly polarised photon beams at the BGO-OD experiment at ELSA*, PhD thesis: Rheinische Friedrich-Wilhelms-Universität Bonn, 2016,  
URL: <http://hdl.handle.net/20.500.11811/6897> (cit. on pp. 18, 19).
- [23] G. Scheluchin,  *$\Lambda(1405)$  photoproduction with the BGO-OD experiment*, PhD Thesis: Rheinische Friedrich-Wilhelms-Universität Bonn, 2020,  
URL: <http://hdl.handle.net/20.500.11811/8373> (cit. on pp. 19–21, 25, 29, 44).
- [24] *BGO Tagging System*, BGOOD Collaboration,  
URL: <https://bgo-od.physik.uni-bonn.de/ExperimentalSetup/Tagger/> (visited on 28/03/2021) (cit. on p. 19).

- 
- [25] S. Alef, *Scintillating fibre detector and kinematic fitting for the BGO-OD experiment*, MA thesis: Rheinische Friedrich-Wilhelms Universität Bonn, 2015, URL: [https://www.hsag.physik.uni-bonn.de/forschung/diplom-doktorarbeiten/diplom-masterarbeiten/Masterarbeit\\_Stefan%20Alef.pdf](https://www.hsag.physik.uni-bonn.de/forschung/diplom-doktorarbeiten/diplom-masterarbeiten/Masterarbeit_Stefan%20Alef.pdf) (cit. on p. 20).
  - [26] B.-E. Reitz, *Coherent bremsstrahlung with the scintillating fiber detector of the BGO-OD tagging system*, MA thesis: Rheinischen Friedrich-Wilhelms-Universität Bonn, 2015, URL: [https://www.hsag.physik.uni-bonn.de/forschung/diplom-doktorarbeiten/diplom-masterarbeiten/Masterarbeit\\_Bjoern-EricReitz.pdf](https://www.hsag.physik.uni-bonn.de/forschung/diplom-doktorarbeiten/diplom-masterarbeiten/Masterarbeit_Bjoern-EricReitz.pdf) (cit. on p. 20).
  - [27] *BGO Target System*, BGOOD Collaboration, URL: <https://bgo-od.physik.uni-bonn.de/ExperimentalSetup/Target/> (visited on 06/05/2021) (cit. on p. 21).
  - [28] *BGO MWPC*, BGOOD Collaboration, URL: <https://bgo-od.physik.uni-bonn.de/ExperimentalSetup/MWPC/> (visited on 12/05/2021) (cit. on p. 22).
  - [29] *Atomic and nuclear properties of bismuth germanate (BGO)*, Particle Data Group, URL: [https://pdg.lbl.gov/2020/AtomicNuclearProperties/HTML/bismuth\\_germanate\\_BGO.html](https://pdg.lbl.gov/2020/AtomicNuclearProperties/HTML/bismuth_germanate_BGO.html) (visited on 06/05/2021) (cit. on p. 22).
  - [30] *BGO Ball*, BGOOD Collaboration, URL: <https://bgo-od.physik.uni-bonn.de/ExperimentalSetup/BgoBall/> (visited on 06/05/2021) (cit. on p. 23).
  - [31] O. Freyermuth, *Studies of  $\omega$  Photoproduction off Proton at the BGO-OD Experiment*, Rheinische Friedrich-Wilhelms-Universität Bonn, 2017, URL: <http://hdl.handle.net/20.500.11811/7263> (cit. on p. 27).
  - [32] J. Allison et al., *Recent developments in Geant4*, *Nucl. Instrum. Meth. A* **835** (2016) 186 (cit. on p. 28).
  - [33] V. L. Kashevarov et al., *Photoproduction of  $\pi^0\eta$  on protons and the  $\Delta(1700)D_{33}$ -resonance*, *The European Physical Journal A* **42** (2009) (cit. on p. 36).
  - [34] S. Alef et al.,  *$K^+\Lambda$  photoproduction at forward angles and low momentum transfer*, *The European Physical Journal A* **57** (2021) 80 (cit. on p. 45).
  - [35] The CBELSA/TAPS Collaboration et al., *High statistics study of the reaction  $\gamma p \rightarrow \pi^0\eta p$* , *Eur. Phys. J. A* **50** (2014) 74, URL: <https://doi.org/10.1140/epja/i2014-14074-1> (cit. on p. 46).

